Contrasting Common Era climate and hydrology sensitivities from paired lake sediment dinosterol hydrogen isotope records in the South Pacific Convergence Zone

Ashley E Maloney[1,2*], Julie N Richey[3], Daniel B Nelson[4], Samantha N Hing[5], David A Sear[6], Jonathan D Hassall[6], Peter G Langdon[6], Ursula Sichrowsky[7], Robert Schabetsberger[8], Atoloto Malau[9], Jean-Yves Meyer[10], Ian W. Croudace[11], Julian P Sachs[1]

[1] University of Washington, School of Oceanography, College of the Environment, Seattle, WA 98195, USA
[2] Princeton University, Department of Geosciences, Guyot Hall, Princeton, NJ 08544, USA
[3] U.S. Geological Survey, St. Petersburg, Florida 33701, USA
[4] Department of Environmental Sciences – Botany, University of Basel, Basel, Switzerland
[5] Department of Civil and Environmental Engineering, University of California, Berkeley, California 94720-1710, USA
[6] University of Southampton, Geography and Environmental Science, Highfield, Southampton SO17 1BJ, UK
[7] Institute of Ecology, University of Innsbruck, Innsbruck, Austria
[8] Department of Environment and Biodiversity, University of Salzburg, 5020 Salzburg, Austria
[9] Service de l'Environnement, BP 294, 98600 Mata 'Utu, 'Uvea, Wallis et Futuna
[10] Délégation à la Recherche, BP 20981, 98713 Papeete, Tahiti, French Polynesia
[11] GAU-Radioanalytical, University of Southampton, National Oceanography Centre, European Way, Southampton, SO14 3ZH, UK
*Corresponding author. Currently at Princeton University, Department of Geosciences, Guyot Hall, Princeton, NJ 08544, USA. E-mail address: amaloney@princeton.edu (A.E. Maloney)

Keywords – Tropical Pacific, SPCZ, Holocene, Paleohydrology, Paleolimnology, Organic geochemistry, Sedimentology, Lakes, Hydrogen isotopes, Dinosterol

Highlights

- SPCZ $\delta^2H_{dinosterol}$ and runoff records indicate a drier Medieval Climate Anomaly
- Accurate interpretations of biomarkers require multiproxy and multisite data
- Low amplitude precipitation variability over past 2 kyr along central SPCZ axis
- Lac Lalolalo $\delta^2H_{dinosterol}$ records reflect hydrology, not climate

This work has been accepted to the journal **Quaternary Science Reviews**
https://doi.org/10.1016/j.quascirev.2022.107421

Abstract

Hydroclimate on ʻUvea (Wallis et Futuna) is controlled by rainfall associated with the South Pacific Convergence Zone (SPCZ), the southern hemisphere's largest precipitation feature. To extend the short observational precipitation record, the hydrogen isotopic composition of the algal lipid biomarker dinosterol ($\delta^2H_{dinosterol}$) was measured in sediment cores from two volcanic crater lakes on ʻUvea. The modern lakes differ morphologically and chemically but both contain freshwater within the photic zone, support phytoplankton communities inclusive of dinosterol-producing dinoflagellates, and experience identical climate conditions. $\delta^2H_{dinosterol}$ values track lake water isotope ratios, ultimately controlled in the tropics by precipitation amount and evaporative enrichment. However, in 88-m-deep Lac Lalolalo a steadily decreasing trend in sedimentary $\delta^2H_{dinosterol}$ values from −227 ‰ around year 988 CE to modern values as low as −303 ‰, suggests this lake's evolution from an active volcanic setting to the present system strongly influenced $\delta^2H_{dinosterol}$ values. Although current hydrology and water isotope systematics may now reflect precipitation and evaporation in this lake, the interaction between these processes and large changes in basin morphology, geochemistry, and hydrology obstruct the recovery of a climate signal from Lac Lalolalo's sedimentary $\delta^2H_{dinosterol}$ records. This work emphasizes the importance of site replication and the use of complementary climate reconstruction tools, especially when using molecular proxies that may be sensitive to more than one environmental parameter. Contrary to its neighbor, duplicate $\delta^2H_{dinosterol}$ records from 23-m-deep Lac Lanutavake varied between −277 ‰ and −297 ‰ and indicate slightly drier conditions during the time-period known as the Medieval Climate Anomaly (MCA, 950 – 1250 CE). The $\delta^2H_{dinosterol}$ signal in Lac Lanutavake was muted compared to published records from ʻUpolu (Samoa) and Efate (Vanuatu) indicating that ʻUvea's location is not as sensitive to precipitation variability at sites farther from the SPCZ central axis. Lithogenic runoff proxies combined with $\delta^2H_{dinosterol}$ support the interpretation of a relatively dry MCA on ʻUvea, ʻUpolu, and Efate, potentially due to less intense precipitation, a contracted, or a more zonally oriented SPCZ.

1. Introduction

The South Pacific Convergence Zone (SPCZ) is the southern hemisphere's largest and most prominent convective feature characterized by intense precipitation extending diagonally from the equatorial western Pacific south-eastwards towards the subtropical central Pacific (**Fig. 1**). With ~40 years of satellite data, synoptic and interannual SPCZ precipitation patterns are well described, however pre-satellite decadal to centennial spatiotemporal variability is not well understood (Brown et al., 2020 and references therein). With 12.1 million people dependent on the SPCZ for freshwater and food security (inclusive of Melanesia, Polynesia, and Micronesian islands Kiribati and Nauru in 2021 (United Nations, 2019)), understanding pre-industrial trends in precipitation variability will better inform prediction and mitigation of future changes to this important climate feature.

Existing proxy-based records of past precipitation in the SPCZ region include speleothem (Maupin et al., 2014; Partin et al., 2013) and coral (Lawman et al., 2020; Linsley et al., 2008, 2006; Ourbak et al., 2006; Tangri et al., 2018) records that reveal substantial high-frequency variability but are either not continuous or are too short to capture the earliest portion of the Little Ice Age (LIA 1450 – 1850 CE) and Medieval Climate Anomaly (MCA 950 – 1250 CE) (time intervals defined by the IPCC (Masson-Delmotte et al.,

2013)). Lipid biomarker and runoff paleoprecipitation proxies stored in sedimentary archives from lakes (Konecky et al., 2013; Sear et al., 2020) and marine settings (Tierney et al., 2010; Toomey et al., 2016) in and near the SPCZ offer an opportunity to extend the length of records in this region and quantify the longer timescale variability in precipitation. Theoretical explanations for observed modern SPCZ precipitation variability invoke ocean-atmosphere forcings (Brown et al. 2020). However, recent attempts to synthesize Pacific-basin paleoproxy data (e.g. Atwood et al., 2021; Higley et al., 2018; Sear et al., 2020) indicate the patterns and mechanisms of tropical precipitation variability are complex and/or that some paleohydrology reconstructions contain unknown biases. Additional records from the SPCZ region are needed to replicate existing paleoreconstructions and to clarify how and why the SPCZ varied in the past.

Tropical hydroclimate reconstructions using lipid biomarker hydrogen isotope ratios rely on the link between fluxes of water though the hydrologic cycle and resulting changes in water isotopic composition (Sachse et al., 2012). In the maritime tropics, the isotopic composition of precipitation largely follows precipitation rates where higher regional precipitation rates result in isotopically depleted rain (Aggarwal et al., 2016; Conroy et al., 2013; Dansgaard, 1964; Kurita, 2013). Surface waters, including lakes that accumulate valuable sedimentary archives, primarily reflect precipitation isotope ratios; imprinted on top of the precipitation signal are the effects of evaporation and non-rain contributions (i.e., stream, groundwater, hydrothermal, or seawater) (Bowen, 2010; Bowen et al., 2019).

Phytoplankton lipids, biomolecules that make up cellular membranes and energy stores, have hydrogen isotope ($^2H/^1H$) ratios that are set by their environmental water (Englebrecht and Sachs, 2005; Maloney et al., 2019; Zhang and Sachs, 2007), and the accumulation and preservation of these lipids in lake sediment offers a tool for reconstructing past hydrology. The dinoflagellate lipid biomarker dinosterol (4a, 23, 24-trimethyl-5a-cholest-22E-en-3β-ol) was targeted for this study since it is highly source-specific and produced by only a limited number of taxa (Volkman, 2005; Volkman et al., 1998, 1993). The hydrogen isotopic composition of this lipid biomarker is expressed as $\delta^2H_{dinosterol}$ ($\delta^2H = [(^2H/^1H)_{sample}/(^2H/^1H)_{VSMOW}] - 1$, VSMOW is Vienna Standard Mean Ocean Water). The $\delta^2H_{dinosterol}$ proxy has enhanced our understanding of late Holocene climate in brackish lakes in Palau (Richey and Sachs, 2016; Sachs et al., 2018; Smittenberg et al., 2011), brackish (Nelson and Sachs, 2016) and freshwater (Atwood and Sachs, 2014) lakes in the Galápagos Islands, and a freshwater lake on Washington Island in the Northern Line Islands (Sachs et al., 2021). An earlier study established that $\delta^2H_{dinosterol}$ values in modern lake sediments throughout the SPCZ region are well correlated with spatial variability in precipitation rates (Maloney et al., 2019), offering an opportunity to make quantitative estimates of precipitation changes in this region; an approach that was recently applied to freshwater SPCZ lakes in Samoa and Vanuatu (Sear et al., 2020) and explored in more detail here.

This work presents new $\delta^2H_{dinosterol}$ records (**Table 1**) from two lakes on ʻUvea (Wallis et Futuna) in the western tropical Pacific to understand how central SPCZ precipitation varied during the late Holocene. Duplicate cores from each lake allow for intra- and inter-lake comparisons and provide important lessons on how unique lake environments influence $\delta^2H_{dinosterol}$ values. We also present records of lithogenic runoff proxies from ʻUvea, Lake Emaotul (Efate, Vanuatu), and higher resolution records from those published from Lake Lanoto'o (ʻUpolu, Samoa) (Gosling et al., 2020), that complement the $\delta^2H_{dinosterol}$ records in the same cores, aiding interpretations of precipitation change within the SPCZ.

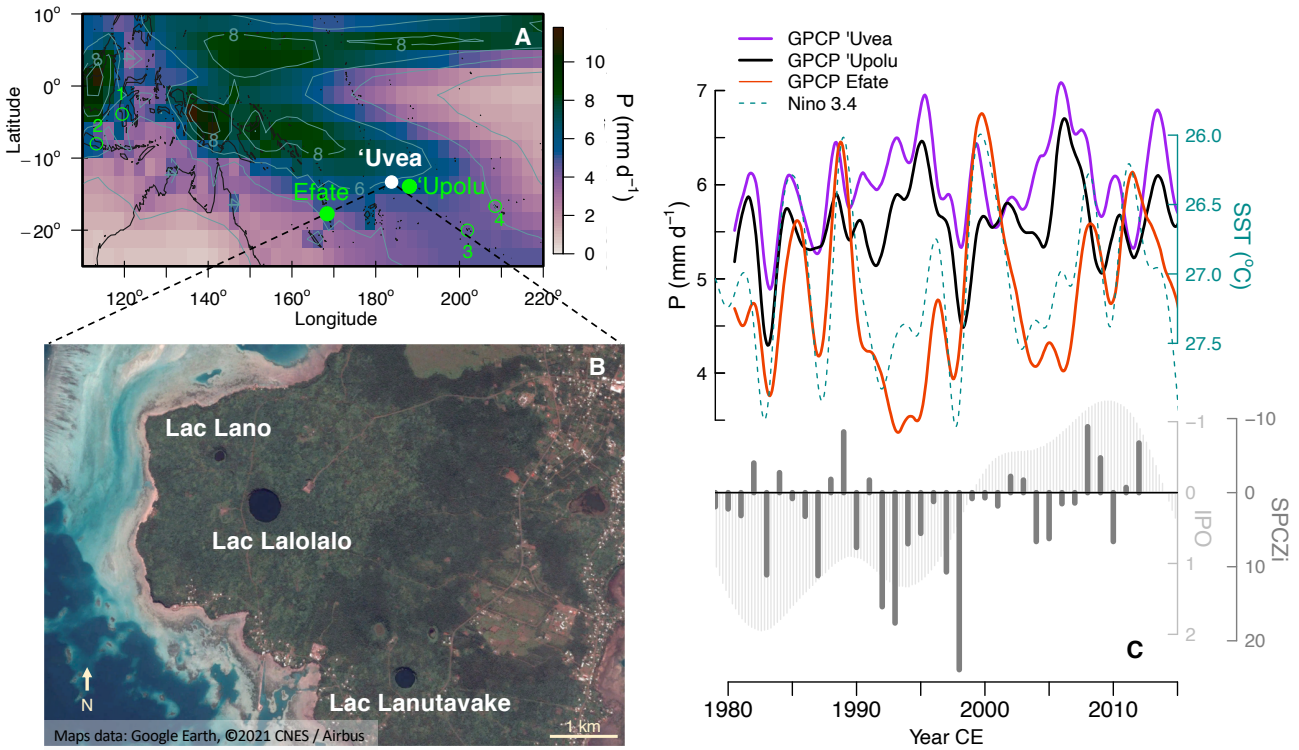

Figure 1. Regional setting. (A) Contours and color scale show mean Global Precipitation Climatology Project (GPCP) precipitation rate (mm d^{-1}) on a 2.5° x 2.5° grid for the 1979 to 2016 period, white dot indicates location of 'Uvea (Wallis et Futuna), filled green dots indicate locations of 'Upolu (Samoa), and Efate (Vanuatu), open green dots indicate locations with $\delta^2H_{leafwax}$ records that extend into the MCA from: 1. the West Sulawesi margin, Indonesia (Tierney et al. 2010), 2. East Java, Indonesia (Konecky et al. 2013), 3. Atiu, Cook Islands (Sear et al. 2020), and a runoff record from 4. Apu Bay, Tahaa French Polynesia (Toomey et al. 2016). (B) Google Earth image of sampled 'Uvea lakes. (C) The upper panel shows 1-yr symmetrically smoothed running means of GPCP precipitation rates at 'Uvea (purple), 'Upolu (black), and Efate (orange) and sea surface temperatures (dotted cyan line, note inverted cyan right y-axis); specifically, each monthly data point was averaged with the 12 months preceding and 12 months following, repeated three times total. The lower panel shows Pacific basin climate indices: the SPCZi index (dark gray bars, Salinger et al., 2014) indicates when the position of the main SPCZ axis is relatively eastward (positive) compared to a westward position (negative), roughly associated with IPO phase (fine light gray bars , Folland et al., 2002), note inverted axis.

2. Regional Setting

'Uvea is the main island of Wallis (French territory of Wallis et Futuna) located in the southeastern region of the SPCZ along its central axis (**Fig. 1**) and influenced by the seasonal and interannual SPCZ migrations (Alory and Delcroix, 1999) with an average Global Precipitation Climatology Project (Adler et al., 2018, 2012, 2003) (GPCPv2.3) (1979–2016) precipitation rate of 6.0 mm d^{-1}. 'Uvea has a large average seasonal [DJF−JJA] precipitation range (5.2 mm d^{-1}) and minor average El Niño-Southern Oscillation (ENSO) [La Niña−El Niño] precipitation variability (0.8 mm d^{-1}) (**Table A.1**). Here El Niño or La Niña conditions are defined as periods when the Oceanic Niño Index, derived from sea surface temperature anomalies in the Niño 3.4 region, is above 0.5 °C or below −0.5 °C following NOAA (2021). Located 480 km to the southeast, 'Upolu (Samoa) has very similar precipitation conditions with an average GPCP precipitation rate of 5.6 mm d^{-1}, large (5.6 mm d^{-1}) seasonal variations, and small ENSO variations where La Niña precipitation rates are 0.7 mm d^{-1} wetter than El Niño conditions. Lake Lanoto'o on 'Upolu is situated in a volcanic crater 760 m above sea level (m.a.s.l.) with a maximum depth of 16.4 m, previously described in detail (Gosling et al., 2020; Parkes, 1994; Sear et al., 2020) and harbors dinosterol-producing

dinoflagellates (Schabetsberger et al., 2021, 2009). To the southwest, Lake Emaotul on the volcanic Efate Island (Ash et al., 1978; Raos and Crawford, 2004) is ~131 m above sea level and experiences fluctuating water depths between 0 and 10 m (Hope, 1996; Schabetsberger et al., 2009); the shallower areas of the lake surrounding the core site were mostly dry between 1994 and 1997 (Sémah and Wirrmann, 2006). Compared to ʻUvea and ʻUpolu, average GPCP precipitation rates are lowest on Efate (4.8 mm d^{-1}) with moderate seasonal variability where austral summers are on average 3.5 mm d^{-1} wetter than winters. Efate experiences larger ENSO variations and mean annual precipitation rates at Efate are better correlated with mean annual Niño 3.4 region sea surface temperatures than ʻUvea or ʻUpolu (**Fig. A.1**). Mean precipitation rates during La Niña events are on average 2.0 mm d^{-1} wetter than El Niño events, occasionally making Efate as wet or wetter than ʻUvea and ʻUpolu during strong La Niña periods (**Fig. 1**). The SPCZ index (SPCZi), a measure of the November−April mean sea level pressure difference between Suva, Fiji and Apia, Samoa (Salinger et al., 2014) describes shifts of the SPCZ position and is reflected in precipitation patterns at these sites. All three islands experience wetter conditions when the SPCZ is shifted westward (La Niña and/or negative SPCZi conditions), and drier conditions when the SPCZ is shifted eastward/equatorward (El Niño and/or positive SPCZi conditions). The observational record indicates that precipitation more closely aligns with Niño 3.4 region sea surface temperature than it does with other climate indices such as the SPCZi and Interdecadal Pacific Oscillation (IPO) (Folland et al., 2002) (**Fig. 1**).

ʻUvea and its surrounding barrier reef belong to the 5 to 23-Myr-old Samoa Ridge capped with Quaternary basaltic flows and pyroclastics less than 0.5-Myr-old. Lac Lalolalo marks an eruptive vent of the youngest tholeiitic flow (and Lac Lanutavake the second youngest) (Price et al., 1991). Lac Lalolalo (88-m-deep) and nearby Lac Lanutavake (25-m-deep) are crater lakes that formed from collapse after eruption of lava and enlarged by phreatic or phreatomagmatic explosions less than a few thousand years ago (based on <0.3 meters of soil covering the flows) (MacDonald, 1945; Stearns, 1945). Outcrops of fresh olivine-phyric basalt surround both lakes. Only 2.75 km apart, these lakes experience identical climate conditions but have different physical and chemical properties (Meisch et al., 2007; Schabetsberger et al., 2009; Sichrowsky et al., 2014). The present-day photic zones (~6 m in Lac Lanutavake and ~4 m Lac Lalolalo) are freshwater, Lac Lalolalo becomes brackish below ~10 m and increases in salinity at depth (Maloney et al., 2019; Sichrowsky et al., 2014). ʻUvea is a low relief island with a maximum elevation of 151 m at Mt. Lulu Fakahega with permeable soils that result in no permanent rivers. The rim of Lac Lalolalo is ~40 m.a.s.l. and the lake surface is ~1 m.a.s.l., the Lanutavake rim is ~67 m.a.s.l. and the lake surface is ~8 m.a.s.l. (Stearns, 1945) (**Fig. A.2**). Daily tidal patterns do not influence the surface level of either lake, which slightly decreased (by ~0.4 and ~0.8 cm d^{-1}) during our visit, May 9 – 22 (2011), the drier part of the season (**Fig. A.3**). There has been no documented damage from tsunamis that have reached ʻUvea. Its barrier and fringing reefs seem to play a role in protecting the island from wave heights greater than two to three meters, although evidence exists for paleotsunamis ~1450 CE and ~0 CE (Lamarche et al., 2015).

Polynesian arrival to ʻUvea is thought to have started as early as 900 – 800 BCE followed by Tongan colonization around 1000 – 1100 and 1400 CE (Lamarche et al., 2015; Sand, 2000, and references therein). Native and introduced agricultural flora (Badré and Hoff, 1995; Kirch, 1978; Meyer, 2017; St. John and Smith, 1971; Stevens, 2018) and fauna (Bareille et al., 2015; Gunkel-Grillon et al., 2015; Meisch et al., 2007; Papazian et al., 2007; Thibault et al., 2015) are found on Wallis et Futuna. While impacts of pig farming have been noted on the soil chemistry on ʻUvea (Gunkel-Grillon et al., 2015), the forest surrounding Lac Lalolalo

has been carefully managed and protected in the past (Guiot, 1998). During our visit we identified plants living directly on the shoreline and within reach from our sampling boat in Lac Lalolalo (**Table A.2**). Lac Lalolalo and Lac Lanutavake waters harbor dinosterol-producing dinoflagellate genera *Peridinium* and *Gymnodinium* (Schabetsberger et al., 2009), in addition to zooplankton (Meisch et al., 2007; Sichrowsky et al., 2014), tilapia (Hinds, 1969; Schabetsberger et al., 2009) and, in Lac Lalolalo, native eels (Bareille et al., 2015). Strontium isotope ratios of otoliths provide clear support that young eels enter Lac Lalolalo from the ocean presumably through small, hidden underground connections (Bareille et al., 2015) and become trapped in the lake as they mature. Details about surface sediments from ʻUvea, ʻUpolu, Efate lakes, including compound-specific isotope analyses and pollen assemblages, have been recently described (Ladd et al., 2021; Maloney et al., 2019) and a preliminary assessment of microfossils in ʻUvea sediment is described in **Appendix A**.

Table 1. Sediment core sites and data summary, "*n.s.*" indicates not suitable since Lac Lalolalo $\delta^2H_{dinosterol}$ values do not track precipitation, "n.d." indicates no data.

Site Name	Latitude	Longitude	Core ID	Water depth at core site	Elevation lake surface	$\delta^2H_{dinosterol}$ min	$\delta^2H_{dinosterol}$ max	n	$\delta^2H_{dinosterol}$ range	Precipitation[3] range	Mag. Sus. signal	Titanium data
	°	°		m	m	‰	‰		‰	mm d^{-1}		
Lac Lalolalo, 'Uvea, Wallis	−13.30108	183.765917	LALOUC13	88	1	−283	−227	36	56	*n.s.*	✓	n.d.
Lac Lalolalo, 'Uvea, Wallis	−13.30048	183.766000	LALOUC14	88	1	−270	−227	30	42	*n.s.*	✓	n.d.
Lac Lalolalo, 'Uvea, Wallis	−13.30168	183.768083	LALOUC22	23	1	−303	−240	7	42	*n.s.*	n.d.	n.d.
Lac Lalolalo, 'Uvea, Wallis	−13.30168	183.768039	LALOUC24	24	1	−292	−242	6	45	*n.s.*	n.d.	n.d.
Lac Lanutavake, 'Uvea, Wallis	−13.32118	183.786033	LATVKUC1	23.3	13	−294	−279	24	16	1.2	✓	n.d.
Lac Lanutavake, 'Uvea, Wallis	−13.32115	183.786133	LATVKUC4	23.2	13	−297	−277	29	20	1.6	✓	n.d.
Lake Lanoto'o, 'Upolu, Samoa[1]	−13.91088	188.172600	LAN14 U2 + L1-1	16.4	760	−290	−255	22	35	2.9	✓	✓
Emaotul Lake, Efate, Vanuatu[1]	−17.72989	168.415462	VAN[2]	6	119	−294	−259	41	35	2.9	✓	✓

[1]Sear et al. 2020, Maloney et al. 2019
[2]Cores/sections: G5, G9, L1, L1A, L2, L2A, L3, L3A. Core top sample includes G7 (0–2 cm), G5 (0–2 cm), and a 0–1cm section collected in 1995 (Maloney et al. 2019)
[3]$[P = (\delta^2H_{sample} + 211) / -12.1]$, GPCP core top calibration (Maloney et al. 2019)

3. Methods

3.1. Sediment sampling and scanning

Sediment from ʻUvea (Wallis et Futuna) was collected from Lac Lalolalo and Lac Lanutavake in May 2011 with a hand-operated check valve coring device (Universal Percussion Corer, Aquatic Research, Hope, ID) with 6.6 cm diameter core liners (2 m maximum length). The uppermost portions (ranging from 0 – 18 cm to 0 – 97 cm) were sectioned in the field at 1 cm intervals (0.5 cm for LATVKUC4) to a depth at which the sediment was sufficiently consolidated to transport without disturbance to stratigraphy (**Table A.3**). If the remaining intact cores were too long for transport, they were cut into two sections, but all ʻUvea cores are single drive cores. Cores collected from 88 m water depth in Lac Lalolalo displayed vigorous degassing in the topmost sediment upon retrieval, mixing stratigraphy in the top 15 to 20 cm. Therefore, the first 15 cm (LALOUC14) or 20 cm (LALOUC13) were sampled in bulk into one bag. Additional cores collected from ~24 m water depth near the shore of Lac Lalolalo (**Fig. A.4**) had intact, unmixed sediment-water interfaces to capture the most recent sedimentary history and the top 16 cm (LALOUC22) or entire 27 cm core (LALOUC24) were sectioned in the field.

ʻUvea cores were split at the University of Washington or at the LacCore facility at the Limnological Research Center (LRC), University of Minnesota. Cores were imaged with a DMT CoreScan and analyzed for magnetic susceptibility at 0.5 cm intervals using a high-resolution point sensor (MS2E) mounted on a GEOTEK XYZMSCL. Magnetic susceptibility data was not acquired for the uppermost portions of sediment cores that were sectioned in the field.

Sampling of the sediment-water interface of Lake Lanoto'o ('Upolu, Samoa) and Lake Emaotul (Efate, Vanuatu) was conducted with a split core tube in a UWITEC gravity corer, the split sealed with gaffer tape. On recovery, excess water was siphoned off and Zorbitrol powder gently added to the remaining 5 cm of water above the sediment to consolidate the uppermost sediments for subsequent transport and sampling. Interface cores were split in the field and a plastic U-channel was impressed into the exposed sediment enabling an undisturbed section to be preserved and transported for analysis. The remaining intact sediment was subsampled in the field at 0.5 – 2 cm intervals. Deeper sediments were collected with a 120 cm Livingstone-type corer (Geo-Core, Columbus, OH). After transport and extrusion into PVC tubing, cores underwent magnetic susceptibility analysis at 1.0 cm intervals. Cores were then split longitudinally and U-channels were taken for micro X-ray fluorescence (μXRF) at 200 μm resolution (500 μm in LAN14-L1-1) at the National Core facility BOSCORF, University of Southampton. The terrestrial in-wash proxy titanium normalized by incoherence scatter (Ti/Inc), as reported in Gosling et al. (2020) and Sear et al. (2020), was used for Lake Emaotul cores and titanium corrected for water (Ti*) for Lake Lanoto'o cores following Boyle et al. (2015). In Lake Lanoto'o the gravity core section LAN14-UC2 and Livingstone-type section LAN14-L1-1 were used as a single composite core. In Lake Emaotul, near core top samples from two undated gravity cores (VANG7 (0 – 2 cm) and VANG5 (0 – 2 cm)) as well as a 0 – 1 cm sample from a core collected in 1995 (Maloney et al., 2019) were combined for a single core top mean $\delta^2H_{dinosterol}$ value, and ages from two additional samples from G5 (2 – 4 cm and 4 – 5 cm) are estimates only. Dated gravity core (VANG9) and Livingstone-type sections (VANL1, VANL1A, VANL2, VANL2A, VANL3, VANL3A) were combined for a single Lake Emaotul record. We used the Ti/Inc data from core sections from Lake Emaotul to update the composite depths of all samples and data that were previously published (Sear et al., 2020), in particular all data from section VANL2 were incorrectly inverted in Sear et al. (2020), the data here represent the correct alignment between sections using the most recent age model which incorporates new ^{14}C dates as well as two new $\delta^2H_{dinosterol}$ values. Note the incorrect alignment of section VANL2 in Sear et al. (2020) does not impact the broader paleoclimate interpretation from that record.

3.2. Chronology

Age models were developed using ^{14}C dates of terrestrial macrofossils and ^{210}Pb analysis of sediments as described in Maloney et al. (2019). Briefly, leaf or plant fossils were pre-treated for radiocarbon analyses with an acid-base-acid procedure (Brock et al., 2010) at the University of Washington before analyses at Direct AMS (Seattle, WA), or CAMS (LLNL, Livermore, CA). All ^{14}C dates for 'Uvea cores are listed in **Table A.4** and age control points for all cores in this manuscript are reported in **Table B.1**. Each of the four sediment cores from Lac Lalolalo has its own age model and is reported and graphed as an independent core. The two cores from Lac Lanutavake were aligned to the same depth scale and share the same age model (**Fig. A.5**). Radiocarbon ages for Lac Lalolalo, Lac Lanutavake, Lake Lanoto'o (Sear et al., 2020), and Lake Emaotul (Sear et al., 2020) were calibrated using SHCal20 (Hogg et al., 2020) and the SH1-2 bomb curve extension (Hua et al., 2013). One new radiocarbon date from Lake Emaotul analyzed at the University of Belfast (UBA) and a date considered an outlier not published in Sear et al. (2020) are included here. Selected sediment intervals from the uppermost sediment (12 to 90 cm) were analyzed for abundance of atmosphere derived ^{210}Pb. All 'Uvea ^{210}Pb results are reported in Maloney et al. (2019) and 'Upolu and Efate results in Sear et al. (2020). Age-depth relationships were constructed using rBACON v2.5.6 package

(Blaauw and Christen, 2011), run settings are specified in **Table B.1**. For all cores the topmost age at 0 cm was assumed to be the same as collection date (± 1 year) and no age control points were omitted from the age model.

3.3. Lipid isotope analyses

Sediment samples consisted of 1 cm intervals, 0.5 cm for the top 39 cm of LATVKUC4, or a homogenized 15 cm or 20 cm sample interval for the disturbed core top portions of LALOUC14 and LALOUC13. To balance resolution and spatial coverage, typical sampling intervals were every two to six cm. Lipids were extracted from freeze-dried sediment samples with an Accelerated Solvent Extractor (ASE-200, Dionex Corp. Sunnyvale, CA, USA) and total lipid extracts were saponified then purified using aminopropyl gel and silica gel column chromatography according to the procedure specified in Maloney et al. (2019). The sterol-containing fraction was acetylated, and dinosterol was HPLC-purified (Nelson & Sachs 2013), identified, quantified, and analyzed for $\delta^2H_{dinosterol}$ at the University of Washington according to previously used methods and instrument settings (Maloney et al., 2019). The average number of sample injections was at least 2.1 times for a core (up to an average of 3.8 injections for a core), and the pooled uncertainties of $\delta^2H_{dinosterol}$ values from each core were between 4.2 ‰ and 6.4 ‰ (Polissar and D'Andrea, 2014; **Tables B.3-B.10**). All dinosterol sample preparation and analyses from 'Uvea, 'Upolu, and Efate sediment were performed in the same lab, and except for two new Lake Emaotul (Efate,Vanuatu) sediment samples from core section VANL2, by the same workers during the same period, minimizing the potential for systematic preparatory artifacts that confound comparisons between sample sets.

3.4. Observational records

The Global Precipitation Climatology Project (GPCPv2.3) gridded satellite-gauge data product (Adler et al., 2018, 2003) was used to compute average annual, seasonal, and ENSO precipitation rates for the 1979 – 2016 period (**Fig. 1, Fig. A.1**, **Fig. A.3, Table A.1**); estimates of precipitation uncertainty are from Adler et al. (2012). The Global Precipitation Climatology Centre (GPCC) gauge data product (Schneider et al., 2018) was used to compare average annual 1951 – 2016 precipitation rates to satellite era rates (**Fig. A.1**). GPCP and GPCC precipitation data are provided by the National Oceanic & Atmospheric Administration/Oceanic & Atmospheric Research/Earth System Research Laboratory Physical Sciences Division (NOAA/OAR/ESRL PSD), Boulder, Colorado, USA, from their website at http://www.esrl.noaa.gov/psd/. The datasets are gridded at a 2.5° x 2.5° scale and based on gauge and/or satellite observations. Smoothed point data extraction from netcdf files was performed in the R programming language using a "bilinear" method to average the four grid cells nearest to each lake site using R (v4.0.5, R Core Team, 2021) with RStudio Desktop (v1.4.1106, RStudio Team, 2021), the raster (Hijmans et al., 2021) and ncdf4 (Pierce, 2019) packages.

Sea surface temperatures from the Niño 3.4 region (Rayner et al., 2003) are from https://psl.noaa.gov/gcos_wgsp/Timeseries/Nino34/. The SPCZi index is from (Salinger et al., 2014) and the IPO index is from (Folland et al., 2002), with the updated version available at http://cola.gmu.edu/c20c/IPO_Aug2017_NZ_UPDATED_FOR_C20C+.pdf.

3.5. Water chemistry

Subsurface waters were collected from Lac Lalolalo, Lac Lanutavake, and Lac Lano with a hand-held Nisken bottle or hand-pump fastened to a weighted tube and filter holder. Samples for water isotope analysis were stored in glass vials sealed to avoid evaporation. Samples for ion and metal analysis were stored in 125 ml HDPE Nalgene bottles, kept in a cooler with an ice pack, and frozen at the end of the collection day. Previously published (Maloney et al., 2019; Sichrowsky et al., 2014) temperature, salinity, and dissolved oxygen measurements are included for comparison and were made *in situ* with a Hydrolab Quanta Water Quality Monitoring System (OTT HydroMet) down to 25 m (the length of the sonde cable) or by submerging the probe into the Nisken bottle upon its return to the surface from depths >25 m.

Lake water isotopes were measured at University of Hawaii on a Picarro L1102-*i* WS-CRDS with analytical precision of 0.5 ‰ for δ^2H and 0.04 ‰ for $\delta^{18}O$ determined using an in-house standard run after every 10th sample. Previously published tap water, rain events, seawater, and lake water isotope data from ʻUvea, Lake Lanotoʻo (ʻUpolu, Samoa), and Lake Emaotul (Efate, Vanuatu) (Maloney et al. 2019) are included for comparison. The mean precipitation isotope climatology at ʻUvea was calculated with the Online Isotopes in Precipitation Calculator version 3.1 (Bowen and Revenaugh, 2003), available at https://wateriso.utah.edu/waterisotopes/pages/data_access/oipc.html, using data from the Global Network of Isotopes in Precipitation (IAEA/WMO, 2021), available at https://nucleus.iaea.org/wiser.

Water samples from 6 depths in Lac Lalolalo were thawed, filtered to remove precipitates, and analyzed for dissolved inorganic nutrients, fluorine, and chlorine using ion chromatography (Dionex DX120); for trace metals using Inductively Coupled Argon Plasma Mass Spectrometry (Thermo Scientific 61E ICP-MS), and carbonate chemistry with a Radiometer Copenhagen PHM85 Precision pH meter equipped with a ABU80 AutoBurette for titration by 0.02 M H_2SO_4 at the University of Washington School of Forestry Analytical Services Center.

4. Results

4.1. Sediment age

Age models (**Table B.1**) reveal that sediment from Lac Lalolalo core LALOUC14 extends back to ~166 BCE, with three of nine ^{14}C dates in core LALOUC14 determined to be outliers, likely due to contributions of pre-aged terrestrial material. Core LALOUC13 had a chronologically harmonious age model with eight ^{14}C dates. The Lac Lalolalo shallow water cores had four to seven ^{210}Pb samples and one to two modern ^{14}C dates. Core top mixing observed in the LALOUC13 0 − 20 cm sample (approximately 1828 to 2011 CE) and LALOUC14 0 − 15 cm sample (approximately 1565 to 2011 CE) precluded meaningful ^{210}Pb analysis in these cores. Lac Lanutavake cores (LATVKUC1, LATVKUC4) did not have enough material for ^{210}Pb analysis. Sediment cores collected from Lac Lanutavake had laminations of tan and brown sediment interspersed with thick layers of dark algal gyttja; similarities in color and excellent similarity between the magnetic susceptibility records in Lac Lanutavake cores allowed them to be visually aligned so that ^{14}C dates could be used from both cores to create a single composite age model (**Fig. A.5**). Using a modified depth scale of LATCKUC1, a total of ten ^{14}C dates were used to create a single BACON age model applied to both cores. The mean age uncertainty for all $\delta^2H_{dinosterol}$ samples from Lac Lalolalo was ± 102 years and from Lac Lanutavake was ± 94 years.

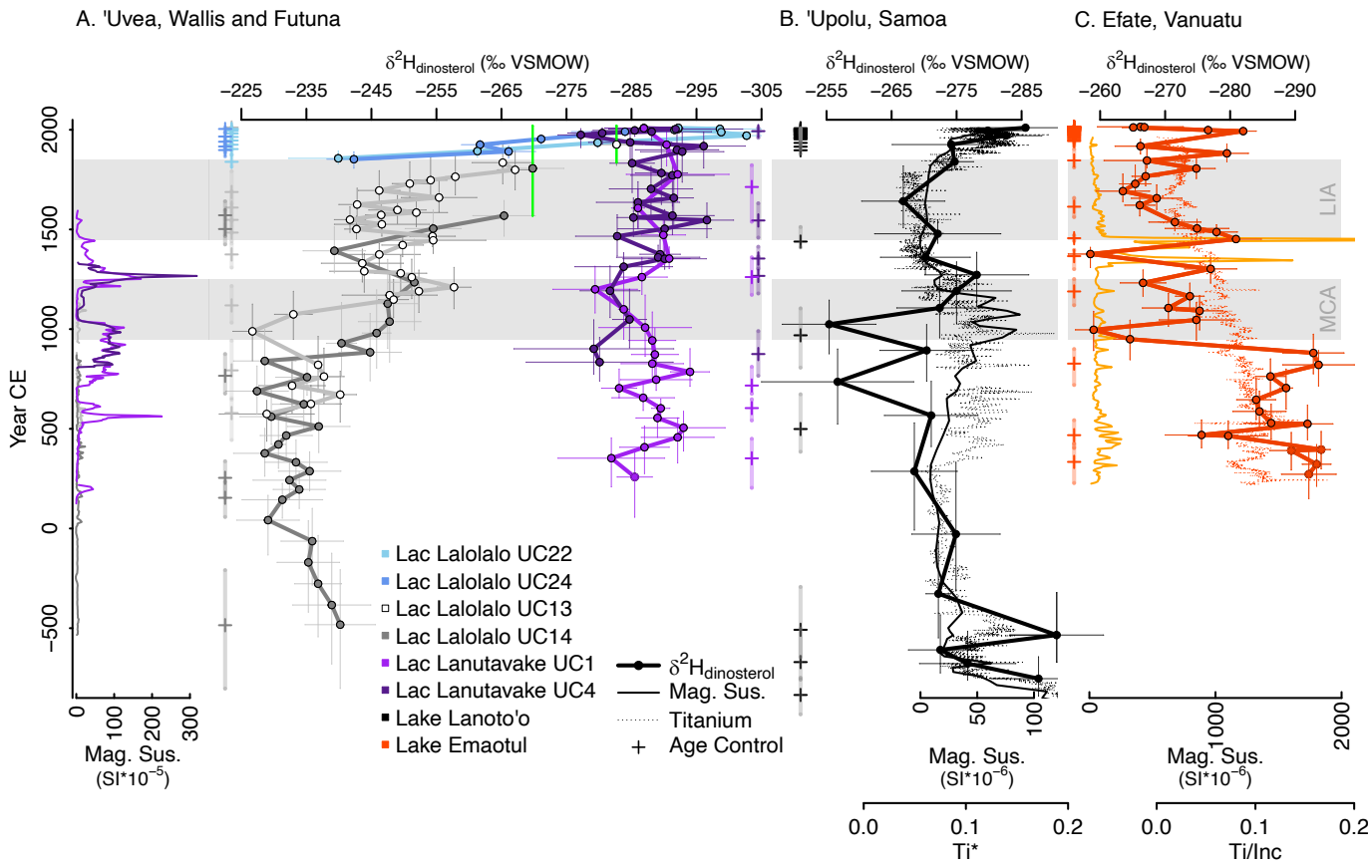

Figure 2. All downcore sedimentary proxy data from ʻUvea (Wallis et Futuna), ʻUpolu (Samoa), and Efate (Vanuatu). (A) Magnetic susceptibility (Mag. Sus.) and $\delta^2H_{dinosterol}$ records from ʻUvea: records from Lac Lalolalo are from two short shallow water cores (blues: UC22 and UC24) and two long deep water cores (grays: UC13 and UC14), the periods covered by the mixed core top samples from UC13 (0 to 15 cm) and UC14 (0 to 20 cm) are highlighted by green vertical lines. Records from nearby Lac Lanutavake are from two cores (purples: UC1 and UC4), note there is no magnetic susceptibility data from the uppermost (field-sectioned) portions of these cores. (B) The $\delta^2H_{dinosterol}$ record from Lake Lanotoʻo (ʻUpolu) (Maloney et al., 2019; Sear et al., 2020) mirrors recent magnetic susceptibility and titanium corrected for water (Ti*) records, diverging during the MCA. (C) Lake Emaotul (Efate) has a $\delta^2H_{dinosterol}$ record (Maloney et al., 2019; Sear et al., 2020) that is mirrored by titanium normalized by incoherence scatter (Ti/Inc) (darker orange) and magnetic susceptibility (lighter orange) (with the exception of the Kuwae ash signal 1350 to 1450 CE). Error bars show analytical uncertainty from multiple injections (x-axis) and BACON age model uncertainties (y-axis) which are omitted from magnetic susceptibility and titanium records for clarity. Crosses indicate age control points with the max/min age estimates as vertical lines behind the crosses (not including three outliers from Lac Lalolalo UC14 and one outlier from Lake Emaotul). Horizontal shading indicates the LIA (1450 to 1850 CE) and MCA (950 to 1250 CE).

4.2. Sedimentary $\delta^2H_{dinosterol}$

All $\delta^2H_{dinosterol}$ data can be found in **Appendix B Tables B.3 – B.10**, ranges are summarized in **Table 1**, and mean values for the modern, LIA, and MCA, and total core mean are summarized in **Table A.5**. Replicate $\delta^2H_{dinosterol}$ records from both lakes on ʻUvea had good intra-lake agreement, but very different inter-lake results (**Fig. 2**). From Lac Lanutavake, LATVKUC1 $\delta^2H_{dinosterol}$ values had a 15 ‰ range from −294 to −279 ‰ (n=24) and LATVKUC4 had a similar 20 ‰ range from −297 to −277 ‰ (n=29). $\delta^2H_{dinosterol}$ values in LATVKUC1 increased by 15 ‰ from −294 ‰ in 790 year CE (+114/−74) to its highest $\delta^2H_{dinosterol}$ value of −279 ‰ in 1199 year CE (+114/−122), returning to relatively lower $\delta^2H_{dinosterol}$ values after 1352 year CE (+49/−54) implying a dry period during the MCA. $\delta^2H_{dinosterol}$ values in

LATVKUC4 also follow a similar MCA pattern but with fewer samples prior to and during the MCA, and a less pronounced change out of the MCA into the LIA. Aside from the oldest two samples in LATVKUC4, $\delta^2H_{dinosterol}$ records appear to echo the magnetic susceptibility records where overlap occurs: dinosterol with relatively higher $\delta^2H_{dinosterol}$ values was deposited during intervals when sedimentary magnetic susceptibility was low (**Fig. A.6**). However, within a single core, Lac Lanutavake $\delta^2H_{dinosterol}$ measurements were not correlated with magnetic susceptibility values from the corresponding sample depths (**Fig. A.7**).

Compared to Lac Lanutavake, Lac Lalolalo had much higher $\delta^2H_{dinosterol}$ values prior to the 20th century, LALOUC13 had a 56 ‰ range from −283 to −227 ‰ (n=36) and LALOUC14 had a 42 ‰ range from −270 to −227 ‰ (n=30). The uppermost samples from these deep-water cores consisted of the top 20 cm of sediment in core LALOUC13 and top 15 cm of sediment in core LALOUC14. The $\delta^2H_{dinosterol}$ values from these homogenized core top samples (−283 ‰ and −270 ‰) overlap with mean values of the intact shallow water short cores that cover the same approximate time periods. LALOUC22 $\delta^2H_{dinosterol}$ values had a 42 ‰ range from −303 to −261 ‰ (n=7) and LALOUC24 had a 45 ‰ range from −288 to −242 ‰ (n=6). Taken together, ranges of $\delta^2H_{dinosterol}$ values in LALOUC13 + LALOUC22 (76 ‰) or LALOUC14 + LALOUC24 (60 ‰) were ~four times larger than in neighboring Lac Lanutavake. While duplicate cores from the same lake agree well, the very different $\delta^2H_{dinosterol}$ records in Lac Lanutavake compared to Lac Lalolalo clearly indicate that one or both lakes was not principally controlled by hydroclimate.

4.3. Runoff proxies

Magnetic susceptibility and titanium runoff signals often reflect in-wash of terrigenous materials from the surrounding watershed when precipitation is heavy or frequent enough to suspend and carry fine particles from the proximal environment (Croudace et al., 2019; Hodell et al., 2008; Liu et al., 2011; Rodysill et al., 2012; Sear et al., 2020). The vertical cliffs surrounding Lac Lalolalo result in a small catchment (restricted almost entirely to the lake surface) and limit the supply of terrigenous runoff, resulting in primarily organic sediments, often containing terrestrial plant debris, and a low and noisy magnetic susceptibility signal (maximum magnetic susceptibility value 26 SI*10^{-5}). Lac Lanutavake is also surrounded by steep walls, but lower and more gradually sloping than Lac Lalolalo (**Fig. A.2, A.4**), creating a relatively more expansive watershed relative to lake diameter. Lac Lanutavake had organic-rich algal gyttja, less plant debris, and yielded large and detailed magnetic susceptibility signals. LATVKUC1 (magnetic susceptibility values up to 226 SI*10^{-5}) and LATVKUC4 (magnetic susceptibility values up to 316 SI*10^{-5}) had very similar magnetic susceptibility patterns (**Fig. 2**). In addition to these two cores selected for further analysis, two nearby cores from Lac Lanutavake (**Fig. A.4**) were analyzed for magnetic susceptibility only: LATVKUC3 (with very similar patterns to LAVTKUC4) and closest to the lake edge, LATVKUC6 which had a distinct feature (magnetic susceptibility values up to 800 SI*10^{-5}) not replicated in the other three cores (**Fig. A.8**).

Runoff proxies from Lake Lanoto'o ('Upolu, Samoa) have been previously reported (Gosling et al., 2020), but only at low resolution for Ti/Inc, now corrected for water content as Ti* after Boyle et al (2015). This work presents the high-resolution Ti* records from the late Holocene sections (LAN14-U2 and LAN14-L1-1) to compare to $\delta^2H_{dinosterol}$ records (Sear et al., 2020). Ti* values were highest (~2.5) around the

MCA, dropping to very low levels (below 0.5) during the LIA, then climbing to 1.0 to 1.5 near the core top. The magnetic susceptibility signal closely tracked the Ti* pattern with values up to 9 SI*10^{-6}. Both the magnetic susceptibility and Ti* records were well-aligned with $\delta^2H_{dinosterol}$ records except during the MCA (**Fig. 2**) when lake levels dropped, changing the physical lake basin. Prior to and after this divergence, magnetic susceptibility and Ti* values were well correlated (R^2 = 0.41 and 0.45, p=0.004 and 0.003) with $\delta^2H_{dinosterol}$ values from same depths (**Fig. A.7; Section 5.2.1 below**).

Lake Emaotul runoff records had Ti/Inc levels that were variable and high (>1.5) in the oldest part of the record, falling to ~0.5 during the MCA, climbing slightly to ~1.0 prior to the LIA, then relatively low and stable from the LIA to the core top (between 0.5 and 0). The magnetic susceptibility signal in this core was typically small but the largest peak around 1440 to 1465 CE had tephra shards geochemically fingerprinted to the Kuwae eruption 105 km north of Lake Emaotul (Sear et al., 2020) that occurred ~1452 − 53 CE or potentially 1458 CE (Abram et al., 2020; Plummer et al., 2012) (**Fig. 2**).

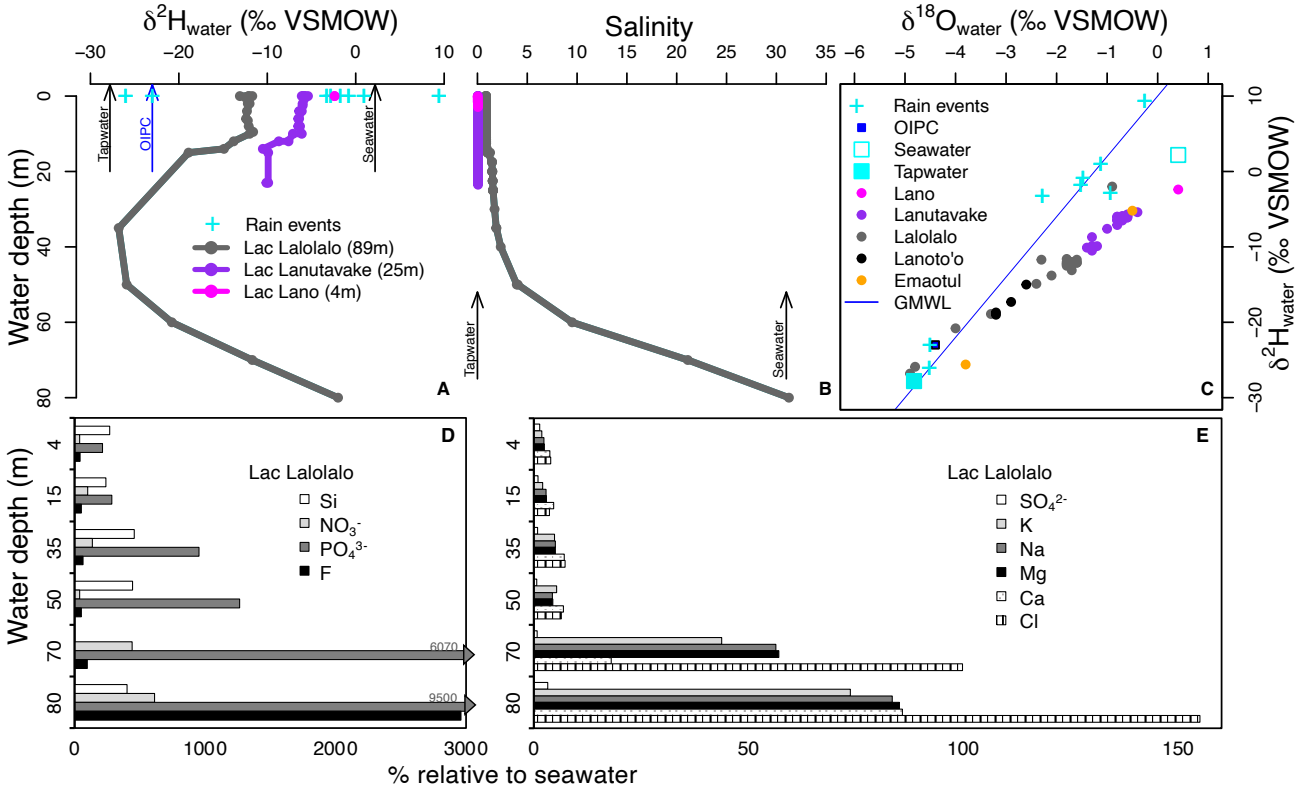

Figure. 3. ʻUvea (Wallis et Futuna) lake water chemistry. (A) Hydrogen isotopic composition of Lac Lalolalo (gray), Lac Lanutavake (purple), and Lake Lano (magenta) water, ʻUvea tap water and surface seawater endmembers are indicated with arrows, rain samples from ʻUvea are indicated with cyan "+" marks, and the annual mean $\delta^2H_{precipitation}$ estimate at ʻUvea from the OIPC3.1 (−23 ± 1 ‰) is indicated with a blue arrow. (B) Salinity values from Lac Lalolalo, Lac Lanutavake, and Lake Lano are bracketed by tap water (salinity = 0) and coastal seawater (salinity = 31) endmembers. (C) $\delta^{18}O_{water}$ versus δ^2H_{water} with the global meteoric water line (y = 8x + 10) and Lake Lanotoʻo (black) and Lake Emaotul (orange) samples for reference. Salinity profiles (Sichrowsky et al., 2014), ʻUvea surface water isotope data, and surface waters from Lake Lanotoʻo and Lake Emaotul have been previously published (Maloney et al., 2019). Analytical uncertainties (omitted for clarity) and are up to 1.3 ‰ for δ^2H_{water} and 0.3 ‰ for $\delta^{18}O_{water}$. Lac Lalolalo ion and metal concentrations relative to mean seawater values including (D) silicon, nitrate, phosphate, and fluoride, and (E) sulfate, potassium, sodium, magnesium, and calcium, and chloride (**Table A.6**).

4.4. 'Uvea Lake Water Chemistry

The hydrogen isotopic composition of lake water (**Fig. 3; Table B.2**) ranged from −5 ‰ to −10.5 ‰ in Lac Lanutavake and −2 ‰ to −27 ‰ in Lac Lalolalo, values bracketed by a surface seawater sample collected from the lagoon (2 ‰) and tap water (sourced from the island's aquifer) (−28 ‰) endmembers. The deepest samples in Lac Lalolalo were isotopically similar to the seawater sample, while mid-depths were very similar to tap water, and surface waters were influenced by evaporation as indicated by their evolution away from the global meteoric water line (**Fig. 3C**).

In Lac Lalolalo potassium, sodium, magnesium, and calcium profiles increased with salinity, implying a contribution of seawater at the deepest depths. However, at 80 m chloride became 1.5 times more concentrated than seawater (**Fig. 3E**) and silicon, nitrate, phosphate, and fluoride became 4 (Si) to 95 (PO_4^{3-}) times more concentrated relative to seawater (**Fig. 3D**). Sulfate was always much less concentrated than seawater. When water from the deepest depths was retrieved by Niskin bottle, it "boiled" upon exposure to atmospheric pressure; hydrogen sulfide was not quantitatively measured but easily detected by odor at depths below (and including) 12 m. Surface nitrate was low, increasing to very high concentrations at depth, while phosphate was extremely high at all depths (indicating eutrophic to hypereutrophic water) (**Table A.6**). Carbonate and bicarbonate data indicate high levels of alkalinity in Lac Lalolalo but titrations were complicated by changes in pH that occurred between collection in Nalgene HDPE bottles, freezing, transport, filtering, and measurement, as well as high organic content and high concentrations of additional ions and should be interpreted as estimates only (**Table A.6**).

5. Discussion

The large range and very high $\delta^2H_{dinosterol}$ values in Lac Lalolalo compared to Lac Lanutavake (**Fig. 4**), combined with the unique geologic setting of Lac Lalolalo indicate that $\delta^2H_{dinosterol}$ records from Lac Lalolalo are unlikely to reflect hydroclimate. Pre-modern $\delta^2H_{dinosterol}$ values from Lac Lalolalo would result in precipitation rates as low as 1.3 mm d^{-1}, in stark contrast to records from Samoa, Vanuatu, Lac Lanutavake, and modern values from Lac Lalolalo (3.7 to 7.6 mm d^{-1}) and up to 20 ‰ more ^{2}H-enriched (as high as −227 ‰) compared to the driest value (−247 ‰) used to create the core top calibration (Maloney et al., 2019). Below we propose possible alternative influences on Lac Lalolalo's $\delta^2H_{dinosterol}$ values and emphasize the need for redundancy and replication when interpreting paleoprecipitation archives. Meanwhile, Lac Lanutavake's $\delta^2H_{dinosterol}$ values appear to record SPCZ hydroclimate and are compared to instrumental, runoff, and $\delta^2H_{dinosterol}$ records from Lake Lanoto'o ('Upolu, Samoa), and Lake Emaotul (Efate, Vanuatu) to support this interpretation.

5.1. High $\delta^2H_{dinosterol}$ values in Lac Lalolalo sediments

Only 2.75 km apart on an island with little topography, Lac Lalolalo and Lac Lanutavake experience identical climate conditions. Modern average core top $\delta^2H_{dinosterol}$ values in both lakes are similar, a small ~5 ‰ difference easily explained by a ~5 ‰ difference in surface $\delta^2H_{lakewater}$ values (Maloney et al., 2019). However, Lac Lalolalo has pre-modern $\delta^2H_{dinosterol}$ values up to 50 ‰ higher than Lac Lanutavake's highest $\delta^2H_{dinosterol}$ value (**Fig. 2**). Major physical, chemical, and/or biological changes must have occurred in Lac Lalolalo to cause such contrary past $\delta^2H_{dinosterol}$ values including 1) changes in salinity and/or past lake water

isotope composition, 2) shifts in dinoflagellate ecology or metabolism, or 3) post depositional alterations to $\delta^2H_{dinosterol}$ values.

Lac Lalolalo's deep modern $\delta^2H_{lakewater}$ values, salinity, and several major ion concentrations (K, Na, Mg, and Ca) approach mean seawater values (**Fig. 3**). However, the 80 m sample also contains ions and elements that far exceed values found in mean Pacific seawater (**Fig. 3**). High levels of fluoride and chloride indicate volcanic inputs of HCl and HF, and our preliminary assessment of high alkalinity could result from volcanic inputs of dissolved inorganic carbon or hydrolysis of Lac Lalolalo's fresh olivine volcanic rocks (Rouwet et al., 2015). High levels of phosphates and nitrates could also result from accumulation of volcanic inputs (González-Vega et al., 2020; Karl et al., 1988), and the potentially high levels of bicarbonate likely enable phosphate accumulation without precipitation (Toner and Catling, 2020). Sulfate levels are very low compared to seawater, likely from bacterial sulfate reduction (forming the hydrogen sulfide smelled below 12 m); high levels of hydrogen sulfide might also come from seawater-rock reactions or magmatic gas inputs during lake formation (Butterfield et al., 2004 and references therein).

Lac Lalolalo's fresh and oxygenated photic zone is the only probable dinosterol-producing region given the strong oxycline at 10 m and the fact that dinosterol-producing dinoflagellates are obligate aerobes. However, it is conceivable that this lake was not always meromictic and/or that surface waters were previously exposed to seawater. The major ion composition of deep lake water provides evidence of past strong volcanic activity which could have impacted water $^2H/^1H$ ratios if volcanic inputs were large enough to mix deep salty and relatively ^2H-enriched water to the surface through vigorous release of gas and hydrothermal water. Additionally, high temperature reactions between some rocks and water can cause ^1H to preferentially partition into the mineral phase (Saccocia et al., 1998). Furthermore, in contrast to the assumption that 'Uvea craters were enlarged by explosions caused by ground water (Stearns, 1945), it is more likely that Lac Lalolalo was "born" salty since a phreatic explosion violent enough to create a lake of this size was almost certainly influenced by seawater. If Lac Lalolalo's modern photic zone was seawater in the past, surface water would be ~12 ‰ higher compared to our 2011 visit. A salinity change from 0 to 30 would have a concomitant dinosterol ^2H-enrichment of 30 ‰ (Nelson and Sachs, 2014; Sachs and Schwab, 2011). At this hypothetical "seawater extreme" condition, higher $\delta^2H_{lakewater}$ values plus increased salinity could contribute a 42 ‰ increase in $\delta^2H_{dinosterol}$ values, which would account for the bulk of the anomalously high $\delta^2H_{dinosterol}$ values in Lac Lalolalo's pre-modern samples.

It is unlikely that tsunamis or storm surge contributed to past surface salinity given Lac Lalolalo's elevation and distance from shore, and there are no large below-surface connections between the lake and the ocean, as evidenced by the lack of tidal influence (**Fig. A.3**). However, the presence of eels in the lake whose otoliths have geochemical fingerprints of ocean water (Bareille et al., 2015), imply passages large enough for elvers (young eels) to transit from the ocean to the lake. Small open passageways between the lake and ocean (likely indirectly via the water table), offer another possible mechanism to introduce seawater to Lac Lalolalo's surface, especially if the island's fresh groundwater diminishes sufficiently during a prolonged drought to allow saltwater intrusion. During the last few thousand years as minerals precipitated and likely constricted, closed, and sealed subsurface seawater connections, Lac Lalolalo basin morphology likely became less permeable to groundwater, seawater from below the Ghyben-Herzberg lens, volcanic degassing, and hydrothermal waters resulting in the hydrological conditions observed today.

Shifts in species composition (e.g., Sessions et al., 1999; Zhang and Sachs, 2007) may also alter the isotopic composition of dinosterol through time. This could occur in unison with changes in salinity if dinoflagellates shifted from a marine to the freshwater community found today. Additionally, environmental shifts may alter the preferred metabolism of metabolically flexible dinosterol-producing dinoflagellates, and a shift from photoautotrophy to heterotrophy can result in large ^{2}H-enrichements up to 165 ‰ in green algae (Estep and Hoering, 1981) and 140 ‰ in bacteria lipids (X. Zhang et al., 2009). Other factors that could cause relative ^{2}H-enrichement of dinosterol in this tropical location include low light (Sachs et al., 2017) if turbidity was higher, or low growth rates (Sachs and Kawka, 2015; Z. Zhang et al., 2009) if nutrient concentrations were lower. Both remain additional possible influences on past higher $\delta^{2}H_{dinosterol}$ values in Lac Lalolalo.

A final possible explanation for very high $\delta^{2}H_{dinosterol}$ values in Lac Lalolalo compared to Lac Lanutavake is post depositional alterations of $\delta^{2}H_{dinosterol}$ values. Schwab et al. (2015) found ^{2}H-enrichement in sedimentary $\delta^{2}H_{dinosterol}$ values was correlated with higher eutrophication. Lac Lalolalo is phosphate-rich, nitrate-rich (except for the surface), and has a shallow Secchi depth – all indicating eutrophic or hypereutrophic conditions, so it is conceivable that post-depositional degradation altered $\delta^{2}H_{dinosterol}$ values in these sediments. Since more recent sediments are in line with expected modern values, this process would only be applicable to the pre-modern sediments. Regardless of the mechanism(s) for past high $\delta^{2}H_{dinosterol}$ values in Lac Lalolalo, the clear differences between Lac Lalolalo and Lac Lanutavake imply that one (or both) of the records cannot be used to make interpretations about past precipitation variability, and highlight the importance of targeting replicate sites to ensure proper interpretation of paleohydroclimate. Therefore precipitation rates calculated from Lac Lalolalo $\delta^{2}H_{dinosterol}$ values prior to ~1950 are not reported (**Tables B.5 to B.8**).

5.2. Hydroclimate from Lac Lanutavake (ʻUvea, Wallis), Lake Lanotoʻo (ʻUpolu, Samoa), and Lake Emaotul (Efate, Vanuatu)

Given the large differences between neighboring lakes on ʻUvea, and the conclusion that Lac Lalolalo is not reliably recording past precipitation rates, this section considers additional proxies and overlapping instrumental data to establish if Lac Lanutavake's sediment records can be considered a robust recorder of precipitation. Lac Lanutavake $\delta^{2}H_{dinosterol}$ and magnetic susceptibility records together with $\delta^{2}H_{dinosterol}$ and runoff records from Lake Lanotoʻo (Samoa) and Lake Emaotul (Vanuatu) provide support for the construction of regional precipitation histories for the SPCZ. We propose that $\delta^{2}H_{dinosterol}$ values at all three sites track $\delta^{2}H_{lakewater}$ values controlled by hydroclimate and $\delta^{2}H_{dinosterol}$ values provide estimates of GPCP-like precipitation rates through the application of a regional core top calibration (Maloney et al., 2019). The $\delta^{2}H_{dinosterol}$ records and runoff proxies at all three sites indicate a drier MCA relative to the mean background conditions (**Fig. 2, Fig. 4A, Fig. 5, Fig. 6, Fig. A.6**).

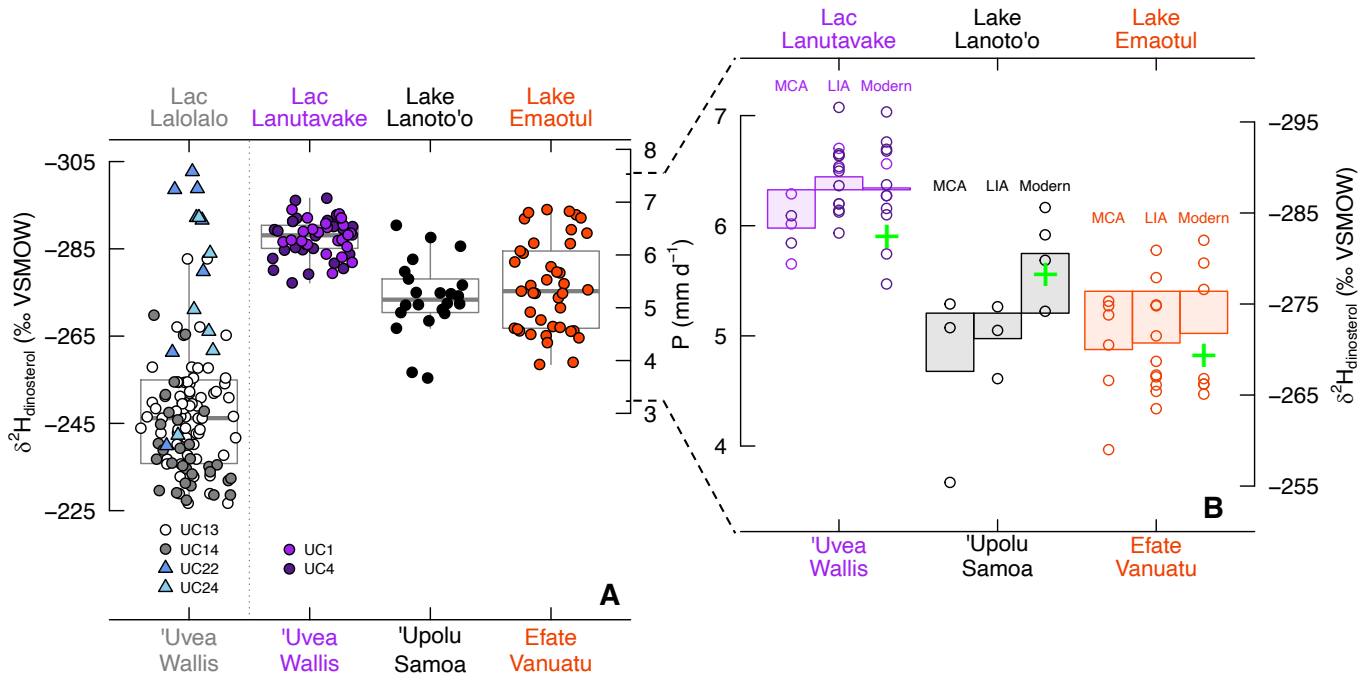

Figure 4. All $\delta^2H_{dinosterol}$ values and corresponding precipitation rates ([P = (δ^2H_{sample} + 211) / −12.1], Maloney et al., 2019) from 'Uvea (Wallis et Futuna), 'Upolu (Samoa), and Efate (Vanuatu). (A) Boxplots of all individual $\delta^2H_{dinosterol}$ data points from Lac Lalolalo's two short cores (blues: UC22 and UC24) and two long cores (grays: UC13 and UC14) (n = 80); Lac Lanutavake's two cores (UC1 and UC4, purples, n = 53); Lake Lanoto'o (black, n = 22), and Lake Emaotul (orange, n = 41). The vertical dotted line separating Lac Lalolalo indicates pre-modern Lac Lalolalo $\delta^2H_{dinosterol}$ values are not primarily influenced by climate and therefore do not have corresponding precipitation rates before ~1950. Gray outline of boxplots is median, upper/lower (75/25%) quartiles, whiskers represent data within 1.5 x interquartile range of upper/lower quartiles. (B) Bar plots of Lac Lanutavake, Lake Lanoto'o, and Lake Emaotul mean MCA, LIA, and modern $\delta^2H_{dinosterol}$ values and corresponding precipitation rates (individual data points as open circles) compared to whole core means represented by horizontal line across all periods (data summarized in **Table A.5**). Green "+" symbols mark gridded GPCP gridded precipitation rates (1979 to 2016 average) (**Table A.1**). Average analytical uncertainty for $\delta^2H_{dinosterol}$ values is 4.7 ‰ (not shown); uncertainties in gridded precipitation are 1.4 mm d^{-1} ('Uvea and 'Upolu) and 0.9 mm d^{-1} (Efate) and uncertainties of reconstructed precipitation (including errors in calibration and analytical uncertainty) are up to 2.5 mm d^{-1} with a mean of 2.2 mm d^{-1} (not shown). Lake Lanoto'o and Lake Emaotul data from Sear et al. (2020) and Maloney et al. (2019).

5.2.1. Runoff records support hydrological interpretations of $\delta^2H_{dinosterol}$ values

Runoff proxies are independently sensitive to precipitation and support interpretations of $\delta^2H_{dinosterol}$ records. Lac Lanutavake is surrounded by more gradual sloping lake walls than Lac Lalolalo with more readily delivered terrigenous material to the lakebed, but likely only during heavy precipitation (**Fig. A.3, A.8**). In Lac Lanutavake, magnetic susceptibility and $\delta^2H_{dinosterol}$ records from duplicate sediment cores display similar patterns throughout most of their temporal overlap (apart from the oldest two $\delta^2H_{dinosterol}$ values from UC4), where high magnetic susceptibility signals are coincident with ^2H-depleted values, providing support that both are responding to hydroclimate in this lake (**Fig. A.6**). In particular, the very low magnetic susceptibility response during the MCA when $\delta^2H_{dinosterol}$ values were relatively higher indicates a period of reduced precipitation.

In Lake Emaotul (Efate, Vanuatu) the Ti/Inc and magnetic susceptibility records (with the exception of the Kuwae ash magnetic susceptibility response **Fig. 2**) very closely tracked variability in $\delta^2H_{dinosterol}$ values (**Fig. 2, Fig. A.7**), providing additional support for hydrological controls on all three

proxies at this site. Lake Lanoto'o ('Upolu, Samoa) is situated atop a volcanic peak (760 m.a.s.l.) with a limited catchment (0.23 km^2), a setting important to consider when interpreting the runoff proxies from this lake. In Lake Lanoto'o the magnetic susceptibility and Ti* signals closely track $\delta^2H_{dinosterol}$ values in the youngest sediment then diverge from the $\delta^2H_{dinosterol}$ record during the MCA. During the MCA the highest $\delta^2H_{dinosterol}$ values imply low precipitation rates while high magnetic susceptibility and Ti* signals conversely suggest high terrigenous inputs. A submerged terrace extending ~10 m out from the current lake shoreline at ~1 m depth offers a nuanced explanation for this disagreement. A drier climate during the MCA likely caused lake level to drop, exposing the lower terrace and effectively increasing the surface area of the lake's watershed (~5% increase in area for a 1 m water drop). A lower lake and larger watershed would decrease the transport distance from shoreline to depocenter so that any precipitation, even less frequent or less intense, would contribute a stronger signal in Ti* and magnetic susceptibility by contributing relatively more terrestrial sediment compared to higher lake-level conditions that submerge more of the catchment.

Linear regressions (**Fig. A.7**) indicate correlations between $\delta^2H_{dinosterol}$ values and corresponding runoff records in Lake Emaotul (Efate, Vanuatu) (excluding the Kuwae ash event in the magnetic susceptibility record, R^2=0.19, p=0.009, n=34), and R^2=0.31, p<0.001, n=36 for Ti/Inc, the largest residuals occur when $\delta^2H_{dinosterol}$ values indicate the driest conditions, which were perhaps accompanied by lake desiccation (and hence reduction of terrestrial magnetics and Ti). Lake Lanoto'o ('Upolu, Samoa) $\delta^2H_{dinosterol}$ values also correlated strongly with corresponding runoff records prior to and after the inferred lower MCA lake level (R^2=0.65, p=0.003, n=17 for Ti* and R^2=0.41, p=0.004, n=18 for magnetic susceptibility). These correlations give us confidence that both $\delta^2H_{dinosterol}$ values and runoff proxies are sensitive to hydroclimate at these sites. There is no significant correlation in Lac Lanutavake data (R^2=0.01, p=0.65, n=25) (**Fig. A.7**). Increased sampling resolution plus magnetic susceptibility data from the upper portions of Lac Lanutavake cores might reveal a stronger correlation. It is also possible that the response of lake water $^2H/^1H$ ratios may be delayed relative to the more immediate response of the magnetic susceptibility record, or the absolute signal of $\delta^2H_{dinosterol}$ may be too small to reveal a correlation if precipitation remained relatively stable on 'Uvea.

5.2.2. Modern $\delta^2H_{dinosterol}$ values track instrumental precipitation

The overall mean modern (1850 to present) reconstructed precipitation rate (6.3±2.3 mm d^{-1}) from Lac Lanutavake $\delta^2H_{dinosterol}$ samples (**Fig. 4, Table A.5**) agrees well with 'Uvea's mean GPCP value (6.0±1.4 mm d^{-1}) (**Table A.1**). Furthermore, **Fig. 5** illustrates how the variability captured in Lac Lanutavake's uppermost six samples echoes the pattern of a smoothed GPCP record within age uncertainties. Smoothing the GPCP record with a 3.5-year running mean approximates how the precipitation signal is reflected in sediment samples of 0.5 to 2 cm thickness that integrate 1 to 8 years of accumulation (average 3.5 years for sites examined here during 1979 to 2016). There are only two (Lake Lanoto'o) or five (Lake Emaotul) samples that overlap with the GPCP record, but their reconstructed precipitation values also approximately match the smoothed instrumental record (**Fig. 5**, **Table A.1, A.5**). Comparing the modern period $\delta^2H_{dinosterol}$ values to the GPCP observational record reveals how slow sediment accumulation rates, low resolution sectioning/sampling, and large age model uncertainties restrict our lacustrine precipitation reconstructions to interannual or longer timescales.

Four aspects of the core top calibration need to be considered when interpreting precipitation estimates generated from $\delta^2H_{dinosterol}$ data. First, $\delta^2H_{dinosterol}$ values most directly reflect $\delta^2H_{lakewater}$ values since biomarker lipids source hydrogen from environmental water with a biosynthetic isotopic fractionation (e.g., Dirghangi and Pagani, 2013; Englebrecht and Sachs, 2005). The $\delta^2H_{lakewater}$ values measured were only snapshots in time (with a seasonal range of up to 20 ‰), so were not directly comparable to the time-integrated $\delta^2H_{dinosterol}$ signal in core top sediments (which may represent up to 20 years). Second, biosynthetic isotopic fractionation values from core top and lake water samples increase with precipitation rate (Maloney et al., 2019), potentially a result of increased nutrient delivery at wetter sites enhancing algal growth rate which can increase biosynthetic isotopic fractionation (Ladd et al., 2018; Sachs and Kawka, 2015). If higher precipitation rates influence growth rate through nutrient delivery, any increased isotopic fractionation serves to amplify the hydrological signal and is embedded in the calibration and downcore $\delta^2H_{dinosterol}$ signal. Third, in lakes where $\delta^2H_{lakewater}$ reflects hydroclimate, P−E (not just P) would better represent the controls on $\delta^2H_{dinosterol}$. However, evaporation rates are similar throughout the SPCZ (Maloney et al., 2019; Yu et al., 2008), more accurate evaporation estimates are not currently available for the core top sites, and the P−E spatial pattern is dominated by P in the tropical Pacific (Schanze et al., 2010). Therefore, applying the calibration assumes that both the P−E relationship and the mean trajectory/source of P is constant through time. Finally, the calibration uses the GPCPv2.3 data set so all estimated precipitation rates should be considered "GPCP-like"; using different rainfall products for a calibration would result in different slopes, intercepts, and uncertainties. Uncertainties in modern $\delta^2H_{lakewater}$ and evaporation make it difficult to quantitatively reconstruct $\delta^2H_{lakewater}$, biosynthetic isotopic fractionation between dinosterol and lake water, or P−E. Therefore this work reconstructs precipitation rates and the agreement at all three sites between GPCP precipitation rates and reconstructed precipitation rates indicates that the core top calibration skillfully captures precipitation rates.

5.2.3. Variable Little Ice Age $\delta^2H_{dinosterol}$ values

After carefully considering all possibilities, the most internally consistent explanation of our multi-proxy dataset from Lac Lanutavake is that it primarily represents a hydroclimate signal, and that it can be interpreted as such together with similarly robust hydroclimate records from Samoa and Vanuatu. Precipitation rates reconstructed from Lac Lanutavake's $\delta^2H_{dinosterol}$ values during the LIA fluctuated between 6 to 7 mm d^{-1}. Wettest conditions occurred in the early LIA and immediately after the LIA, creating a "u-shaped" pattern (**Fig. 5**), with the average of all LIA $\delta^2H_{dinosterol}$ values slightly lower (i.e., wetter) than the core mean (**Fig. 4B**). A more pronounced mid-LIA drying pattern appears in the Lake Lanoto'o and Lake Emaotul $\delta^2H_{dinosterol}$ records, with corresponding reconstructed precipitation rates fluctuating between 4.3 to 5.8 mm d^{-1} and mirrored by runoff records in the same cores (**Fig. 2**). Simple linear regressions from the driest LIA point to present indicate only Lake Lanoto'o had a significant trend towards wetter modern conditions for all proxies measured (**Fig. A.9**). High-resolution coral (Linsley et al., 2006) and cave records (Maupin et al., 2014; Partin et al., 2013) from various locations in the SPCZ also hint at a drier LIA compared to the present, but the changes were too small to confidently attribute to precipitation, or were additionally influenced by factors unrelated to precipitation (e.g., ocean currents, Dassié et al., 2018). To the west of the SPCZ a very clear transition from a drier LIA to wetter modern conditions was observed in

Lake Lading (8ºS, 113º E) (East Java, Indonesia), interpreted as a strengthening of the Walker circulation leading to wetter conditions (Konecky et al., 2013). Changes in Walker circulation strength could also explain the slightly (~1.5 mm d^{-1}) wetter conditions in the late-LIA/modern compared to a dry mid-LIA in Lake Lanoto'o by changing the shape, size, or intensity of SPCZ precipitation. However, this would have to occur without largely changing precipitation on 'Uvea and Efate unless non-climatic factors mute precipitation signals at these locations. A recent reevaluation of tropical Pacific climate changes during the LIA find support for a strengthened Pacific Walker Circulation, but additional records from the central and eastern tropical Pacific are needed (Atwood et al., 2021).

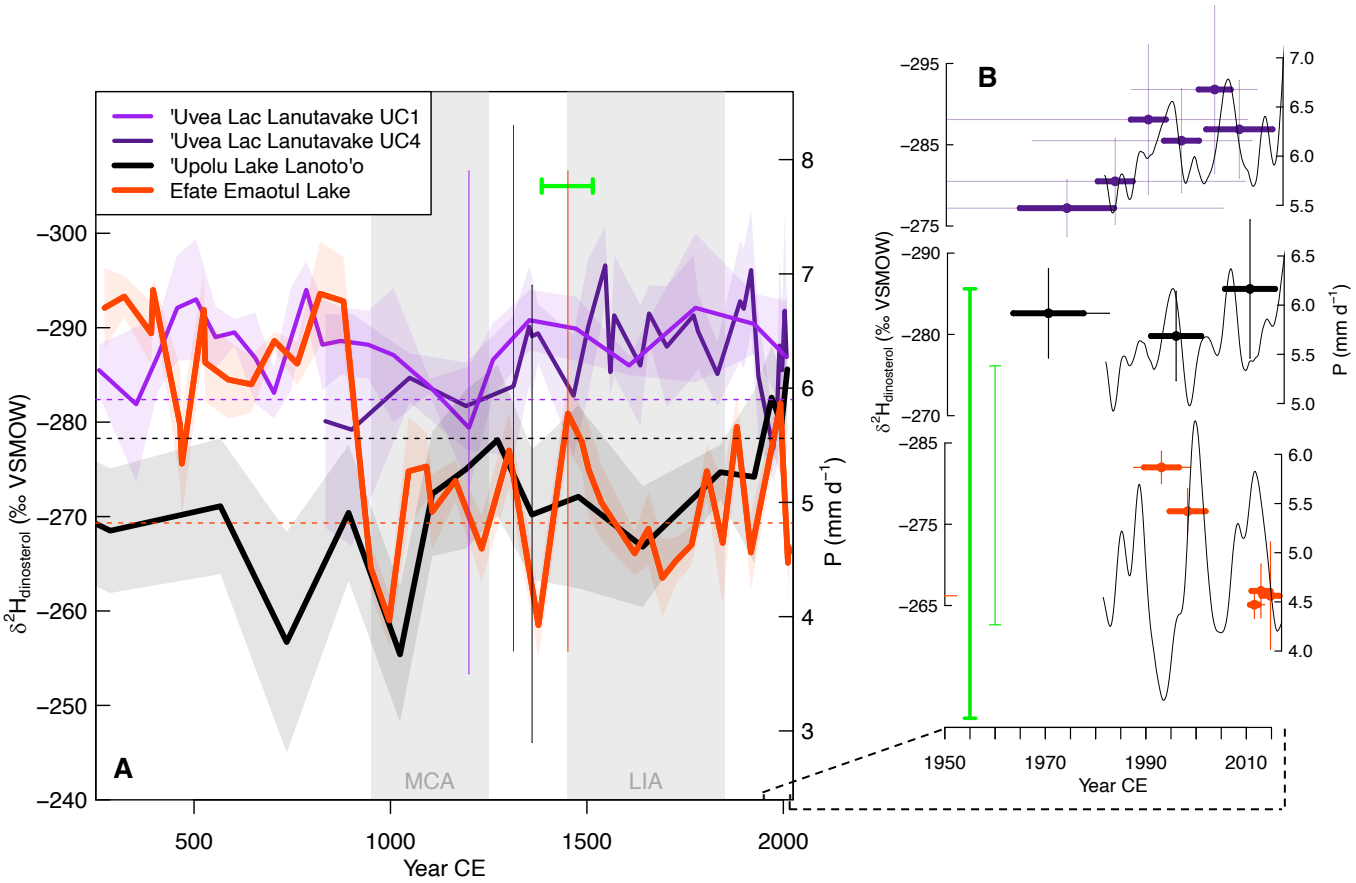

Figure 5. $\delta^2H_{dinosterol}$ records from Lac Lanutavake ('Uvea, Wallis et Futuna), Lake Lanoto'o ('Upolu, Samoa), and Lake Emaotul (Efate, Vanuatu) with corresponding reconstructed precipitation rates ([P = (δ^2H_{sample} + 211) / −12.1], Maloney et al., (2019)). (A) SPCZ precipitation records during the Common Era, shading around solid lines indicates $\delta^2H_{dinosterol}$ value analytical uncertainty, uncertainties associated with reconstructed precipitation rates (including errors in calibration and analytical uncertainty) are up to 2.5 mm d^{-1} in these cores; for clarity uncertainty for only one sample from each core is shown as a thin vertical line, average age model uncertainty is indicated with a horizontal green bar, shaded gray vertical bars indicate MCA and LIA, and horizontal dashed lines are mean gridded GPCP precipitation rates (1979 to 2017) at each location, these have estimated errors of 1.4 mm d^{-1} ('Uvea and 'Upolu) and 0.9 mm d^{-1} (Efate) (not shown) (**Table A.1**). (B) The same data for the 1950 to 2017 period with 3.5-year running mean gridded GPCP precipitation time series shown as thin black lines (3.5 years is the average accumulation time represented by each sample that overlaps with gridded GPCP data). Thin error bars represent age model uncertainty (x axis) and analytical uncertainty of $\delta^2H_{dinosterol}$ values (y axis); thick horizontal bars represent the time integrated by each sample (1 to 8 years). The thick vertical green bar represents the average reconstructed precipitation rate error (± 2.2 mm d^{-1}), and the thin green vertical bar represents the average GPCP precipitation rate error (± 1.2 mm d^{-1}). $\delta^2H_{dinosterol}$ records from Lake Lanoto'o and Lake Emaotul from Sear et al. (2020); core top samples are from multiple core tops (Maloney et al., 2019).

5.2.4. Drying of ʻUvea, ʻUpolu, and Efate during the Medieval Climate Anomaly

Three $\delta^2H_{dinosterol}$ records indicate MCA drying relative to mean conditions throughout the SPCZ, with the smallest change in Lac Lanutavake on ʻUvea (**Fig. 4B, Fig. 5**). The driest MCA values from Efate, Vanuatu (4.0±1.8 mm d^{-1}) and ʻUpolu, Samoa (3.7±1.7 mm d^{-1}) were 1.4 to 1.5 mm d^{-1} drier (17 to 19 ‰ higher) compared to their core means. Lac Lanutavake's driest MCA value (5.7±2.2 mm d^{-1}) was only 0.6 mm d^{-1} drier (8 ‰ higher) compared to its mean, 0.8 to 0.9 mm d^{-1} less drying compared to Lake Emaotul and Lake Lanotoʻo (**Fig. 4B**). There are two possible explanations for the smaller change in Lac Lanutavake including 1) a muted response to drying due to a potential connection to ʻUvea's aquifer, and 2) a relatively stable precipitation rate through time at ʻUvea compared to ʻUpolu and Efate.

All 53 samples from Lac Lanutavake have less variability around the mean compared to 41 samples from Lake Emaotul and 22 samples in Lake Lanotoʻo (**Fig. 4**). Modern lake water $^2H/^1H$ profiles indicate two distinct water masses in Lac Lanutavake: a photic zone influenced by evaporation with higher $\delta^2H_{lakewater}$ values (−5 ‰) and bottom water with lower $\delta^2H_{lakewater}$ values (−10 ‰) approaching ʻUvea's aquifer values (−28 ‰) (**Fig. 3**), suggesting a (past and/or present) connection between Lac Lanutavake and ʻUvea's groundwater. The degree to which Lac Lanutavake is a surface expression of ʻUvea's aquifer might play a role in muting lake water isotopic variability (and therefore variability in $\delta^2H_{dinosterol}$ measurements) through time. Mixing between Lac Lanutavake's surface waters and ʻUvea's aquifer could dampen the depletion/enrichment effects of precipitation/evaporation on $\delta^2H_{lakewater}$ since groundwater does not experience extensive evaporative enrichment, groundwater recharge is biased towards heavy (^2H-depleted) rainfall events/seasons (e.g., Li et al., 2018), and groundwater $^2H/^1H$ ratios from Tutuila (American Samoa), an island with similar geology to ʻUvea, are stable around −20 ‰ despite large (~60 ‰) seasonal shifts in $\delta^2H_{precipitation}$ (Shuler et al., 2019). Since Lac Lanutavake's magnetic susceptibility records more clearly indicate a dry MCA, it is possible that a lake-groundwater connection at this site results in a dampening of $\delta^2H_{lakewater}$ (and therefore $\delta^2H_{dinosterol}$) values.

Alternatively, ʻUvea's location along the central SPCZ axis may be responsible for the smaller MCA drying signal detected in Lac Lanutavake compared to Efate and ʻUpolu. Using ENSO variability as an example, today both ʻUvea and ʻUpolu occupy a climatic null zone which experiences little precipitation variability associated with ENSO compared to Efate (Vanuatu) whose rainfall patterns closely track SSTs in the Niño 3.4 region (**Fig. 1, Fig. A.1**). It is possible that ʻUvea has remained in a null zone throughout the last 2000 years while the zone may have passed over ʻUpolu. A recent coral record from Samoa provides evidence of a shifting null zone during the past 600 years (Tangri et al., 2018), and even precipitation gauge records indicate that ʻUpolu's precipitation has been correlated with ENSO in the past, but not during the satellite era (**Fig. A.1**). If ʻUvea's location precludes it from experiencing large ENSO variability, it is conceivable that ʻUvea could also be the least sensitive location to longer timescale variability. Indeed, Lac Lanutavake's $\delta^2H_{dinosterol}$ values are relatively steady throughout the entire 2000-year record, and available gridded instrumental data clearly indicates that ʻUvea experiences less seasonal and interannual variability than ʻUpolu and Efate (**Fig. 1**). This, combined with the responsive magnetic susceptibility signals, leads us to favor ʻUvea's central position as an explanation for its lower variability during the MCA (and potentially LIA), as opposed to possible time-varying inputs of groundwater. Long-term monitoring of lake water

chemistry in Lac Lanutavake and other lakes on ʻUvea could help validate the magnitude of past precipitation change.

From the MCA to the present, Lake Lanotoʻo and Lake Emaotul have nearly identical precipitation rate estimates and similar patterns of variability (i.e., where the thick solid orange and black lines overlap in **Figure 5**). Prior to the MCA, precipitation rates were similar in Lake Emaotul and Lac Lanutavake ~0 to 900 CE (i.e., where the thick solid orange and purple lines overlap in **Figure 5**). This overlap implies that Efate was as wet as ʻUvea before the MCA and drier like ʻUpolu after the MCA. This is unexpected given the higher modern climatological precipitation rate on ʻUvea and ʻUpolu versus Efate (thin dashed horizontal lines in **Figure 5**), and the observations that Efate is rarely as wet as ʻUpolu and ʻUvea (for instance during some La Niña events, **Figure 1**). Comparing the precipitation rate reconstructions from all three locations indicates that the precipitation estimates inferred from $\delta^2H_{dinosterol}$ values may be most useful in a relative sense (comparing variability at a single site) as opposed to an absolute sense (comparing values between sites hundreds of kilometers apart). Tracking additional lake-specific physical and ecological factors that influence $\delta^2H_{lakewater}$, such as the extent of vegetation cover over shallow lakes that can act as a barrier to evaporation (Ladd et al., 2021; Maloney et al., 2019), may be necessary to confidently compare reconstructed precipitation rates across space. Another consideration is that evaporation rates and/or the observed relationship between precipitation amount and the isotopic composition of precipitation may vary through time. If this happened, then the application of a core top calibration could over- or under-estimate quantitatively reconstructed pre-instrumental precipitation rates. This is another reason why it is important to consider runoff proxies that do not rely on the stationarity of isotopic relationships as part of a multi-proxy approach. Finally, if pre-modern SPCZ precipitation rates are accurately captured by the reconstructed patterns presented here, this could result from local scale precipitation shifts (e.g., Atwood et al., 2020), highlighting the need for multiple records from each region.

5.3. Late Holocene SPCZ Precipitation Variability

Three SPCZ $\delta^2H_{dinosterol}$ records from Lac Lanutavake (ʻUvea, Wallis et Futuna), Lake Emaotul (Efate, Vanuatu), and Lake Lanotoʻo (ʻUpolu, Samoa) offer an opportunity to understand long term drivers of SPCZ GPCP-like precipitation rate variability. Each core has unique high-frequency $\delta^2H_{dinosterol}$ changes, different ranges in reconstructed precipitation rates, and distinct correlations with available runoff data. These differences likely result from the diverse environmental settings of each lake, variable sampling intervals, changes in the source and transport of precipitation, local precipitation/evaporation rate shifts, and large-scale changes in SPCZ position or intensity that differentially impact each location. Site and proxy replication is required for interpreting local versus regional scale precipitation rate changes. While all records from ʻUpolu indicate a drier mid-LIA, duplicate $\delta^2H_{dinosterol}$ records from ʻUvea's Lac Lanutavake and records from Efate's Lake Emaotul are relatively stable across the LIA (**Fig. A.9**). Currently there is no site or proxy replication during the LIA from ʻUvea, making it difficult to confidently interpret local versus large scale SPCZ behavior. Additional records that capture LIA runoff in Lac Lanutavake, or cores from ʻUvea's Lake Lano, would be valuable for understanding the nature of SPCZ variability during the LIA before invoking detailed ocean-atmospheric forcings during this period.

Where long-term trends do agree across several sites, especially during the MCA when multiple proxies at each site indicate a dry period, a large-scale change in SPCZ intensity or position can more

confidently be considered. Below our SPCZ runoff and $\delta^2H_{dinosterol}$ records are compared to other paleoclimate records across the Pacific to understand possible mechanistic changes in SPCZ shape and strength.

Spatially extensive paleoenvironmental records that capture the MCA in **Figure 6** show hydroclimate anomalies relative to their means to accommodate different absolute responses to precipitation. The similarities among these records indicate that a relatively drier MCA occurred in the SPCZ and beyond, highlighted by a gray vertical bar from 950 to 1250 in **Figure 6**. To the west of the SPCZ, a sustained MCA dry period was found in Indonesian lake sediment (Konecky et al., 2013), marine sediment (Tierney et al., 2010) (**Fig. 6B-C**), speleothems (Griffiths et al., 2016), and drying inferred from a cultural sequence in Papua New Guinea (Shaw et al., 2020). Dry conditions during the MCA in the SPCZ and Indonesia are noteworthy in light of the coincidence of SPCZ zonal events and Makassar straight salinities (Linsley et al., 2017) suggesting common mechanisms for the changes in and near the SPCZ. Along the southeast margin of the SPCZ, a lake sediment record indicates the Southern Cook Islands were also drier (Sear et al., 2020) (**Fig. 6D**) while a runoff record from French Polynesia indicates an overall wetter MCA (**Fig. 6E**), with two periods of relative drying within the MCA ~ 950 to 1050 and 1150 to 1250 CE (Toomey et al., 2016). Far to the east of the SPCZ, a period of drought is inferred from drying out of lakes on Easter Island during the MCA (Rull, 2021).

A dry MCA at these locations could represent a reduction in rainfall intensity, a reduction in SPCZ extent, or a northeastward shift of the mean SPCZ position such that it collapsed towards the equator into a more zonal position. An equatorward-shifted SPCZ is an orientation supported by drought atlases based on tree-ring networks from an Australia-New Zealand-Indonesia cluster compared to a Mexico-southern United States-western Guatemala cluster (Higgins et al., 2020). While this drought atlas is based on sites far from the SPCZ regions and contains no tropical tree ring data, which brings into question the applicability of its conclusions to SPCZ sites, the two largest westward/equatorward shifts in the Higgins et al. (2020) reconstructed SPCZ index occur during the MCA (gold sections in **Fig. 6A**) and may reflect orientations similar to zonal SPCZ positions observed during some strong El Niño events (1982/83 and 1997/98), as well as the 1991/92 moderate event (Vincent et al., 2011). It is important to note that the two largest eastward/poleward shifts in the tree-ring data also occur during the MCA (green sections in **Fig. 6A**), raising the possibility that the MCA may be more appropriately considered a period of greater and more intense variability between very dry and very wet conditions. Yet very wet MCA conditions are not evident in the SPCZ lake records. Sear et al (2020) postulated a northeastward shift of the SPCZ based on the drier conditions inferred from the Emaotul and 'Upolu records with relatively wetter conditions in French Polynesia from Apu Bay (Toomey et al. 2016). The relative drying observed in Lac Lanutavake's magnetic susceptibility and $\delta^2H_{dinosterol}$ records (**Fig. 6F-G**), while minor, lends support to this pattern of change.

Brown et al. (2020) synthesized the current understanding of the physical mechanisms responsible for modern SPCZ position and strength. Equatorward propagation of Rossby waves from the Southern Hemisphere's subtropical jet trigger diagonally oriented convection; the sum of this convective activity results in the mean SPCZ position which is strongest during the austral summer when the zonal sea surface temperature gradient and oceanic heat content are greatest (Matthews, 2012; van der Wiel et al., 2016, 2015; Widlansky et al., 2011). SPCZ precipitation is also directly forced by heating and tropical convection over the Maritime Continent (Kodama, 1999; Matthews et al., 1996). Finally, moisture-laden low-level air

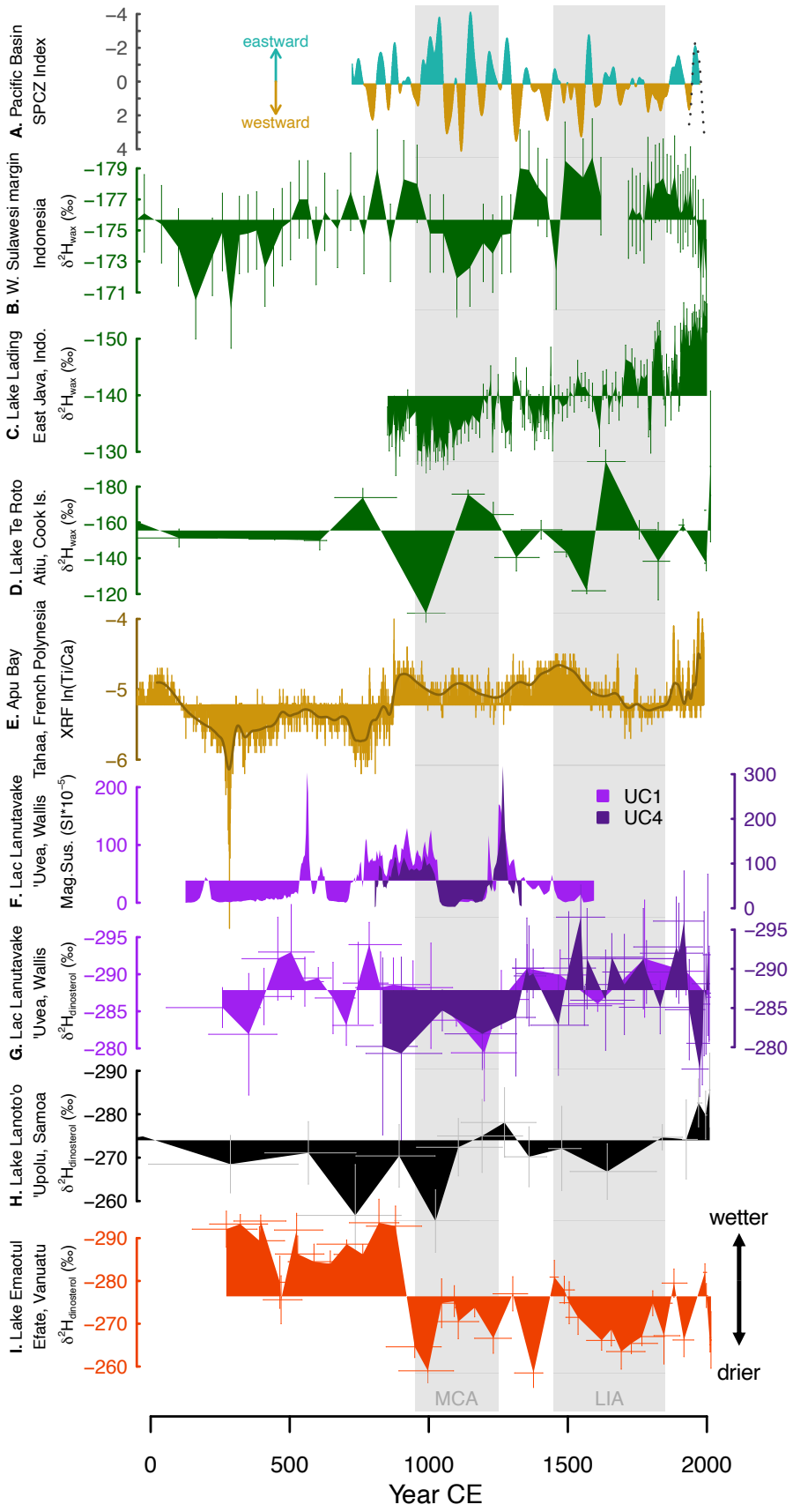

Figure 6. Comparison of Lac Lanutavake $\delta^2H_{dinosterol}$ and magnetic susceptibility records to the SPCZ Index, biomarker records, and a runoff record from the southwestern Pacific. Values at the top of each panel (more negative isotope values, higher magnetic susceptibility values, and natural logarithm ratios closer to zero) indicate periods of relatively higher precipitation. (A) A 50-year gaussian filter applied to the SPCZ index (dotted black line Salinger et al., 2014) and the SPCZ index reconstructed from tree rings (teal and gold segments, Higgins et al., 2020) reflects the relative position of the SPCZ (note inverted axis), (B) δ^2H_{wax} from C_{30} *n*-alkanoic acid from terrestrial leaf wax inputs measured in marine sediments from the W. Sulawesi margin of Indonesia (Tierney et al., 2010), (C) δ^2H_{wax} from C_{28} *n*-alkanoic acid from terrestrial leaf wax inputs measured in Lake Lading sediment (Konecky et al., 2013), (E) XRF ln(Ti/Ca) runoff record (gold) with a 100-yr low pass filter (dark gold) from Apu Bay off the island of Tahaa in French Polynesia (Toomey et al., 2016), (D) δ^2H_{wax} from C_{26} *n*-alkanoic acid from terrestrial leaf wax inputs measured in Lake Te Roto sediment (Sear et al., 2020). (F) Lac Lanutavake UC1 and UC4 magnetic susceptibility (not available for the uppermost material sectioned in the field) and $\delta^2H_{dinosterol}$ (G) records from 'Uvea (this study), and $\delta^2H_{dinosterol}$ records from Samoa (Sear et al., 2020) (H), and Vanuatu (Sear et al., 2020) (I). Error bars indicate uncertainty in age models (x-axis, when provided) and analytical uncertainty (y-axis); note different y-axis scales.

supplied by the Southeastern Pacific's subtropical high contributes to the formation of the SPCZ (Lintner and Neelin, 2008; Takahashi and Battisti, 2007a, 2007b). The diagonal SPCZ orientation results from the combination of these ocean-atmosphere forcings that respond to variations in the background state on observed intraseasonal to interdecadal timescales. Variability in the same forcings may also be responsible for the long-term centennial-scale precipitation changes documented in the sediment cores presented here, possibly even driven by changes in extra-tropical modes of variability such as Multidecadal Atlantic Variability and the IPO (Wang et al., 2017; Zhang et al., 2019). Evidence for MCA drying in the central Pacific (Wyman et al., 2021), east Pacific (Atwood and Sachs, 2014; Conroy et al., 2008; Nelson and Sachs, 2016), and Mesoamerica (Bhattacharya et al., 2015; Curtis et al., 1996; Hodell et al., 2005; Medina-Elizalde et al., 2010; Metcalfe et al., 2010), supports the suggestion of a Pacific-Atlantic teleconnection (e.g. Fig. 6 in Wyman et al. 2021). Available paleoprecipitation records indicate the ocean-atmosphere mechanisms responsible for past hydroclimate variability in the tropical Pacific are not always coherent (Atwood et al., 2021; Higley et al., 2018; Sear et al., 2020) so continued development of multiproxy records in and around the SPCZ should help clarify how and why SPCZ precipitation varied prior to the instrumental record.

6. Conclusion

This study presents a multi-proxy, multi-record dataset based on $\delta^2H_{dinosterol}$ and magnetic susceptibility data spanning the last 2000 years, with full record replication in two individual basins. Records include sediment sequences from two crater lakes, Lac Lalolalo and Lac Lanutavake, on the island of 'Uvea (Wallis et Futuna) and updated $\delta^2H_{dinosterol}$ records and lithogenic runoff proxies from Efate (Vanuatu) and updated runoff proxies from 'Upolu (Samoa). The assessment of moisture changes on 'Uvea is complicated by contradictory $\delta^2H_{dinosterol}$ results in Lac Lalolalo and Lac Lanutavake. We propose that Lac Lalolalo, the youngest and largest volcanic crater lake on 'Uvea, only recently evolved to its current state characterized by fresh surficial water and deeper saline, nutrient-rich, alkaline water. Changes in lake morphology, volcanic hydrochemistry, ecology, or biomarker degradation may explain Lac Lalolalo's evolution from high to low $\delta^2H_{dinosterol}$ values in a manner unrelated to climate. Lac Lanutavake $\delta^2H_{dinosterol}$ records display much smaller changes through time, and we consider this record to reflect hydroclimate. Independent runoff records support interpretations of past change based on $\delta^2H_{dinosterol}$ values; the coherent variations in $\delta^2H_{dinosterol}$ values and magnetic susceptibility in Lac Lanutavake indicate $\delta^2H_{dinosterol}$ values reflect precipitation and reveal a dry MCA. The 'Upolu and Efate runoff records also indicate a dry MCA as their previously published $\delta^2H_{dinosterol}$ records have indicated. During the LIA, conditions appear to be drier than modern on 'Upolu, but 'Uvea and Efate had greater variability and no coherent LIA precipitation change. Multi-proxy analysis of multiple records from the same region are highly valuable for interpreting hydroclimate variability. A large spatial distribution of hydroclimate records is key for understanding regional versus local precipitation changes throughout the SPCZ domain and helps reveal mechanisms responsible for natural tropical precipitation change. The available data imply that these three sites do capture large scale regional variability when they agree, and together they suggest the SPCZ was either less intense (indicating a less vigorous rising limb of the Pacific Walker Circulation), or shifted equatorward away from these sites (resembling the position observed during some strong and moderate El Niño events) during the LIA and MCA compared to the modern, with the driest conditions of the last ~2000 years occurring at some point within the MCA. The mechanisms responsible for the SPCZ shape and size today may be useful for

understanding why the SPCZ changes on longer timescales once common patterns of change are established. A larger network of sites that record past precipitation conditions should help distinguish how the shape and/or intensity of the SPCZ changed in the past.

Acknowledgements

This material is based upon work supported by the US National Science Foundation under Grant Nos. 0823503 and 1502417 to J.P.S. A University of Washington Program on Climate Change Fellowship, IGERT Ocean Change Fellowship [grant #NSF1068839], Princeton University Department of Geosciences Harry H. Hess postdoctoral Fellowship, and Simons Foundation Fellowship [732763] provided partial research support for A.E.M; IGERT Ocean Change mini-research awards, and a University of Washington Quaternary Research Center research award to A.E.M. The Explorers Club Exploration Fund Grant, Gilchrist Expedition Grant and Royal Geographical Society (with IBG) Monica Cole Grant assisted with Samoa travel. Lake Lanoto'o data was funded under a NERC Studentship to J.D.H. Funding for Lake Emaotul research was provided by Natural Environment Research Council (NERC) Grant NE/N006674/1. UBA ^{14}C date was funded by a NERC SPITFIRE PhD Scholarship and sampled by Nichola Strandberg. We are grateful for permission from Wallis civic and traditional authorities. Sample collection in 'Uvea benefitted from the assistance of K. Manufeki, S. Tauvale, C. Manry and others from Service de L'Environment, M. Fotuaika, J.-F. Poncet, P. Nicomette, S. Felomaki, P. Tauvale, C. Chauvet, and the planning assistance from C. Lique, M. Bridoux, and C. Altman. Field work in 'Upolu, Samoa was kindly permitted by Taule'ale'ausmai Laavasa Malua, Chief Executive Officer, Niualuga Evaimalo and staff in Ministry Natural Resources and Environment; field assistance was provided by Josie Hill, Lucy, Tinifu, Solomano and Ai. Tom Bishop assisted with field work on Vanuatu. M. Wolfshorndl, T. Magee, J. Rodysill, and K. Brady assisted with splitting and scanning cores at LacCore. We thank C. Kaapu-Lyons, N. Wallsgrove, and B. Popp for analyzing Wallis water samples. T. Fonville performed the preliminary assessment of microfossils. M. Wolhowe and J. Gregerson assisted with instrument maintenance and M. Wolhowe made two new Vanuatu $\delta^2H_{dinosterol}$ measurements. D. Xue analyzed ions and metals in Lac Lalolalo samples. Conversations with L. Thompson, S. PoChedley, R. Echols, J. Scheff, S. Rushley, D. Battisti, R. Wood, K. Thirumalai, N. Williams, W.J. D'Andrea and constructive comments from A.E. Ingalls, and P. Quay greatly improved this manuscript. Any use of trade, firm, or product names is for descriptive purposes only and does not imply endorsement by the U.S. Government. We thank S.N. Ladd for providing careful feedback on this project and helpful edits on the manuscript. We thank Editor P. Rioual and two anonymous reviewers for their helpful and constructive comments that improved this work.

References

Abram, N.J., Wright, N.M., Ellis, B., Dixon, B.C., Wurtzel, J.B., England, M.H., Ummenhofer, C.C., Philibosian, B., Cahyarini, S.Y., Yu, T.L., Shen, C.C., Cheng, H., Edwards, R.L., Heslop, D., 2020. Coupling of Indo-Pacific climate variability over the last millennium. Nature 579, 385–392. doi:10.1038/s41586-020-2084-4

Adler, R.F., Gu, G., Huffman, G.J., 2012. Estimating climatological bias errors for the global precipitation climatology project (GPCP). J. Appl. Meteorol. Climatol. 51, 84–99. doi:10.1175/JAMC-D-11-052.1

Adler, R.F., Huffman, G.J., Chang, A., Ferraro, R., Xie, P.-P., Janowiak, J., Rudolf, B., Schneider, U., Curtis, S., Bolvin, D., Gruber, A., Susskind, J., Arkin, P., Nelkin, E., 2003. The Version-2 Global Precipitation

Climatology Project (GPCP) Monthly Precipitation Analysis (1979–Present). J. Hydrometeorol. 4, 1147–1167. doi:10.1175/1525-7541(2003)004<1147:TVGPCP>2.0.CO;2

Adler, R.F., Sapiano, M.R.P., Huffman, G.J., Wang, J.J., Gu, G., Bolvin, D., Chiu, L., Schneider, U., Becker, A., Nelkin, E., Xie, P., Ferraro, R., Shin, D. Bin, 2018. The Global Precipitation Climatology Project (GPCP) monthly analysis (New Version 2.3) and a review of 2017 global precipitation. Atmosphere 9. doi:10.3390/atmos9040138

Aggarwal, P.K., Romatschke, U., Araguas-Araguas, L., Belachew, D., Longstaffe, F.J., Berg, P., Schumacher, C., Funk, A., 2016. Proportions of convective and stratiform precipitation revealed in water isotope ratios. Nat. Geosci. 9, 624–629. doi:10.1038/ngeo2739

Alory, G., Delcroix, T., 1999. Climatic variability in the vicinity of Wallis, Futuna, and Samoa islands (13-15°S, 180°-170°W). Oceanol. Acta 22, 249–263. doi:10.1016/S0399-1784(99)80050-4

Atwood, A.R., Battisti, D.S., Wu, E., Frierson, D.M.W., Sachs, J.P., 2021. Data-Model Comparisons of Tropical Hydroclimate Changes Over the Common Era. Paleoceanogr. Paleoclimatology 36, 1–30. doi:10.1029/2020PA003934

Atwood, A.R., Donohoe, A., Battisti, D.S., Liu, X., Pausata, F.S.R., 2020. Robust longitudinally-variable responses of the ITCZ to a myriad of climate forcings. Geophys. Res. Lett. 20, 98–99. doi:10.1029/2020GL088833

Atwood, A.R., Sachs, J.P., 2014. Separating ITCZ- and ENSO-related rainfall changes in the Galápagos over the last 3 kyr using D/H ratios of multiple lipid biomarkers. Earth Planet. Sci. Lett. 404, 408–419. doi:doi: 10.1016/j.epsl.2014.07.038

Badré, F., Hoff, M., 1995. Les Ptéridophytes des Iles Wallis et Futuna (Pacifique Sud): écologie et répartition. Feddes Repert. 106, 271–290.

Bareille, G., Sasal, P., Mary, N., Meunier, F.J., Deschamps, M.H., Berail, S., Pecheyran, C., Lecomte-Finiger, R., 2015. Are elemental and strontium isotopic microchemistry of otolith and histomorphometrical characteristics of vertebral bone useful to resolve the eel *Anguilla obscura* status in Lalolalo lake in Wallis Island? Vie Milieu 65, 29–39.

Bhattacharya, T., Byrne, R., Böhnel, H., Wogau, K., Kienel, U., Ingram, B.L., Zimmerman, S., 2015. Cultural implications of late holocene climate change in the Cuenca Oriental, Mexico. Proc. Natl. Acad. Sci. 112, 1693–1698. doi:10.1073/pnas.1405653112

Blaauw, M., Christen, J.A., 2011. Flexible paleoclimate age-depth models using an autoregressive gamma process. Bayesian Anal. 6, 457–474. doi:10.1214/11-BA618

Bowen, G.J., 2010. Isoscapes: Spatial Pattern in Isotopic Biogeochemistry. Annu. Rev. Earth Planet. Sci. 38, 161–187. doi:10.1146/annurev-earth-040809-152429

Bowen, G.J., Cai, Z., Fiorella, R.P., Putman, A.L., 2019. Isotopes in the water cycle: Regional- to global-scale patterns and applications. Annu. Rev. Earth Planet. Sci. 47, 453–479. doi:10.1146/annurev-earth-053018-060220

Bowen, G.J., Revenaugh, J., 2003. Interpolating the isotopic composition of modern meteoric precipitation. Water Resour. Res. 39, 1–13. doi:10.1029/2003WR002086

Boyle, J.F., Chiverrell, R.C., Schillereff, D., 2015. Approaches to Water Content Correction and Calibration for μXRF Core Scanning: Comparing X-ray Scattering with Simple Regression of Elemental Concentrations, in: Croudace, I.W., Rothwell, R.G. (Eds.), Micro-XRF Studies of Sediment Cores, Applications of a Non-Destructive Tool for the Environmental Sciences. Springer, Dordrecht, pp. 373–390. doi:10.1007/978-94-017-9849-5_14

Brock, F., Higham, T., Ditchfield, P., Ramsey, C.B., 2010. Current pretreatment methods for AMS radiocarbon dating at the Oxford Radiocarbon Accelerator Unit (ORAU). Radiocarbon 52, 103–112. doi:10.1017/S0033822200045069

Brown, J.R., Lengaigne, M., Lintner, B.R., Widlansky, M.J., van der Wiel, K., Dutheil, C., Linsley, B.K., Matthews, A.J., Renwick, J., 2020. South Pacific Convergence Zone dynamics, variability and impacts in a changing climate. Nat. Rev. Earth Environ. 1, 530–543. doi:10.1038/s43017-020-0078-2

Butterfield, D.A., Roe, K.K., Lilley, M.D., Huber, J.A., Baross, J.A., Embley, R.W., Massoth, G.J., 2004. Mixing, reaction and microbial activity in the sub-seafloor revealed by temporal and spatial variation in diffuse flow vents at axial volcano. Geophys. Monogr. Ser. 144, 269–289. doi:10.1029/144GM17

Conroy, J.L., Cobb, K.M., Noone, D., 2013. Comparison of precipitation isotope variability across the tropical Pacific in observations and SWING2 model simulations. J. Geophys. Res. Atmos. 118, 5867–5892. doi:10.1002/jgrd.50412

Conroy, J.L., Overpeck, J.T., Cole, J.E., Shanahan, T.M., Steinitz-Kannan, M., 2008. Holocene changes in eastern tropical Pacific climate inferred from a Galápagos lake sediment record. Quat. Sci. Rev. 27, 1166–1180. doi:10.1016/j.quascirev.2008.02.015

Curtis, J.H., Hodell, D.A., Brenner, M., 1996. Climate variability on the Yucatan Peninsula (Mexico) during the past 3500 years, and implications for Maya cultural evolution. Quat. Res. 46, 37–47. doi:10.1006/qres.1996.0042

Croudace, I.W., Löwemark, L., Tjallingii, R., Zolitschka, B., 2019. Current perspectives on the capabilities of high resolution XRF core scanners. Quat. Int. doi:10.1016/j.quaint.2019.04.002

Dansgaard, W., 1964. Stable isotopes in precipitation. Tellus 16, 436–468.

Dassié, E.P., Hasson, A., Khodri, M., Lebas, N., Linsley, B.K., 2018. Spatiotemporal variability of the South Pacific Convergence Zone fresh pool eastern front from coral-derived surface salinity data. J. Clim. 31, 3265–3288. doi:10.1175/JCLI-D-17-0071.1

Dirghangi, S.S., Pagani, M., 2013. Hydrogen isotope fractionation during lipid biosynthesis by *Haloarcula marismortui*. Geochim. Cosmochim. Acta 119, 381–390. doi:10.1016/j.gca.2013.05.023

Englebrecht, A.C., Sachs, J.P., 2005. Determination of sediment provenance at drift sites using hydrogen isotopes and unsaturation ratios in alkenones. Geochim. Cosmochim. Acta 69, 4253–4265. doi:10.1016/j.gca.2005.04.011

Estep, M.F., Hoering, T.C., 1981. Stable hydrogen isotope fractionations during autotrophic and mixotrophic growth of microalgae. Plant Physiol. 67, 474–477. doi:10.1104/pp.67.3.474

Folland, C.K., Renwick, J.A., Salinger, M.J., Mullan, A.B., Nin, E., 2002. Relative influences of the Interdecadal Pacific Oscillation and ENSO on the South Pacific Convergence Zone 29, 2–5.

González-Vega, A., Fraile-Nuez, E., Santana-Casiano, J.M., González-Dávila, M., Escánez-Pérez, J., Gómez-Ballesteros, M., Tello, O., Arrieta, J.M., 2020. Significant release of dissolved inorganic nutrients from the shallow submarine volcano Tagoro (Canary Islands) based on seven-year monitoring. Front. Mar. Sci. 6, 1–15. doi:10.3389/fmars.2019.00829

Gosling, W.D., Sear, D.A., Hassall, J.D., Langdon, P.G., Bönnen, M.N.T., Driessen, T.D., van Kemenade, Z.R., Noort, K., Leng, M.J., Croudace, I.W., Bourne, A.J., Kemenade, Z.R. Van, McMichael, C.N.H., 2020. Human occupation and ecosystem change on Upolu (Samoa) during the Holocene. J. Biogeogr. 47, 600–614. doi:10.1111/jbi.13783

Griffiths, M.L., Kimbrough, A.K., Gagan, M.K., Drysdale, R.N., Cole, J.E., Johnson, K.R., Zhao, J., Cook, B.I., Hellstrom, J.C., Hantoro, W.S., 2016. Western Pacific hydroclimate linked to global climate variability over the past two millennia. Nat. Commun. 7, 1–9. doi:10.1038/ncomms11719

Guiot, H., 1998. Forêt taboue et représentations de l'environnement à 'Uvea (Wallis). Approche ethno-archéologique. J. Soc. Ocean. 107, 179–198. doi:10.3406/jso.1998.2057

Gunkel-Grillon, P., Roth, E., Laporte-Magoni, C., Le Mestre, M., 2015. Effects of long term raw pig slurry inputs on nutrient and metal contamination of tropical volcanogenic soils, Uvéa Island (South Pacific). Sci. Total Environ. 533, 339–346. doi:10.1016/j.scitotenv.2015.06.110

Higgins, P.A., Palmer, J.G., Turney, C.S.M., Andersen, M.S., Cook, E.R., 2020. One thousand three hundred years of variability in the position of the South Pacific Convergence Zone. Geophys. Res. Lett. 47, e2020GL088238. doi:10.1029/2020GL088238

Higley, M.C., Conroy, J.L., Schmitt, S., 2018. Last millennium meridional shifts in hydroclimate in the central tropical Pacific. Paleoceanogr. Paleoclimatology 33, 354–366. doi:10.1002/2017PA003233

Hijmans, R.J., Etten, J. van, Cheng, J., Baston, D., Bevan, A., Bivand, R., Busetto, L., Canty, M., Fasoli, B., Forrest, D., Ghosh, A., Golicher, D., Gray, J., Greenberg, J.A., Hiemstra, P., Hingee, K., KArney, C., Mattiuzzi, M., Mosher, S., Naimi, B., Nowosad, J., Pebesma, E., Lamigueiro, O.P., Racine, E.B., Rowlingson, B., Shortridge, A., Venables, B., Wueest, R., 2021. raster: Geographic Data Analysis and Modeling. R package version 3.4-10.

Hinds, V.T., 1969. A fisheries reconnaissance to Wallis Island, South Pacific Commission, Nouméa, New Caledonia.

Hodell, D.A., Anselmetti, F.S., Ariztegui, D., Brenner, M., Curtis, J.H., Gilli, A., Grzesik, D.A., Guilderson, T.J., Müller, A.D., Bush, M.B., Correa-Metrio, A., Escobar, J., Kutterolf, S., 2008. An 85-ka record of climate change in lowland Central America. Quat. Sci. Rev. 27, 1152–1165. doi:10.1016/j.quascirev.2008.02.008

Hodell, D.A., Brenner, M., Curtis, J.H., 2005. Terminal Classic drought in the northern Maya lowlands inferred from multiple sediment cores in Lake Chichancanab (Mexico). Quat. Sci. Rev. 24, 1413–1427. doi:10.1016/j.quascirev.2004.10.013

Hogg, A.G., Heaton, T.J., Hua, Q., Palmer, J.G., Turney, C.S.M., Southon, J., Bayliss, A., Blackwell, P.G., Boswijk, G., Bronk Ramsey, C., Pearson, C., Petchey, F., Reimer, P., Reimer, R., Wacker, L., 2020. SHCal20 Southern Hemisphere calibration, 0-55,000 years cal BP. Radiocarbon 62, 759–778. doi:10.1017/RDC.2020.59

Hope, G.S., 1996. Fieldwork Report: A reconnaissance survey of potential sites for pollen analysis in Southern Vanuatu. Unpublished report to Vanuatu Cultural Centre. (Corrections 2017).

Hua, Q., Barbetti, M., Rakowski, A.Z., 2013. Atmospheric radiocarbon for the period 1950-2010. Radiocarbon 55, 2059–2072. doi:10.2458/azu_js_rc.v55i2.16177

IAEA/WMO, 2021. International Atomic Energy Agency/World Meteorological Organization. Global Network for Isotopes in Precipitation, The GNIP Database. Accessible at: http://www.iaea.org/wiser.

Karl, D.M., McMurtry, G.M., Malahoff, A., Garcia, M.O., 1988. Loihi Seamount, Hawaii: A mid-plate volcano with a distinctive hydrothermal system. Nature 335, 532–535. doi:10.1038/335532a0

Kirch, P.V., 1978. Indigenous agriculture on Uvea (Western Polynesia). Econ. Bot. 32, 157–181. doi:10.1007/BF02866870

Kodama, Y.M., 1999. Roles of the atmospheric heat sources in maintaining the subtropical convergence zones: an aqua-planet GCM study. J. Atmos. Sci. 56, 4032–4049. doi:10.1175/1520-0469(1999)056<4032:ROTAHS>2.0.CO;2

Konecky, B.L., Russell, J.M., Rodysill, J.R., Vuille, M., Bijaksana, S., Huang, Y., 2013. Intensification of southwestern Indonesian rainfall over the past millennium. Geophys. Res. Lett. 40, 386–391. doi:10.1029/2012GL054331

Kurita, N., 2013. Water isotopic variability in response to mesoscale convective system over the tropical ocean. J. Geophys. Res. Atmos. 118, 10,376-10,390. doi:10.1002/jgrd.50754

Ladd, S.N., Maloney, A.E., Nelson, D.B., Prebble, M., Camperio, G., Sear, D.A., Hassall, J.D., Langdon, P.G., Sachs, J.P., Dubois, N., 2021. Leaf Wax Hydrogen Isotope s as a Hydroclimate Proxy in the Tropical Pacific. J. Geophys. Res. Biogeosciences 126, e2020JG005891. doi:10.1029/2020jg005891

Ladd, S.N., Nelson, D.B., Schubert, C.J., Dubois, N., 2018. Lipid compound classes display diverging hydrogen isotope responses in lakes along a nutrient gradient. Geochim. Cosmochim. Acta 237, 103–119. doi:10.1016/j.gca.2018.06.005

Lamarche, G., Popinet, S., Pelletier, B., Mountjoy, J., Goff, J., Delaux, S., Bind, J., 2015. Scenario-based numerical modelling and the palaeo-historic record of tsunamis in Wallis and Futuna, Southwest Pacific. Nat. Hazards Earth Syst. Sci. 15, 1763–1784. doi:10.5194/nhess-15-1763-2015

Lawman, A.E., Quinn, T.M., Partin, J.W., Thirumalai, K., Taylor, F.W., Wu, C.C., Yu, T.L., Gorman, M.K., Shen, C.C., 2020. A Century of Reduced ENSO Variability During the Medieval Climate Anomaly. Paleoceanogr. Paleoclimatology 35, 1–17. doi:10.1029/2019PA003742

Li, J., Pang, Z., Kong, Y., Wang, S., Bai, G., Zhao, H., Zhou, D., Sun, F., Yang, Z., 2018. Groundwater isotopes biased toward heavy rainfall events and implications on the local meteoric water line. J. Geophys. Res. Atmos. 123, 6259–6266. doi:10.1029/2018JD028413

Linsley, B.K., Kaplan, A., Gouriou, Y., Salinger, M.J., DeMenocal, P.B., Wellington, G.M., Howe, S.S., 2006. Tracking the extent of the South Pacific Convergence Zone since the early 1600s. Geochemistry, Geophys. Geosystems 7, 1–15. doi:10.1029/2005GC001115

Linsley, B.K., Wu, H.C., Rixen, T., Charles, C.D., Gordon, A.L., Moore, M.D., 2017. SPCZ zonal events and downstream influence on surface ocean conditions in the Indonesian Throughflow region. Geophys. Res. Lett. 44, 293–303. doi:10.1002/2016GL070985

Linsley, B.K., Zhang, P., Kaplan, A., Howe, S.S., Wellington, G.M., 2008. Interdecadal-decadal climate variability from multicoral oxygen isotope records in the South Pacific Convergence Zone region since 1650 A.D. Paleoceanography 23, 1–16. doi:10.1029/2007PA001539

Lintner, B.R., Neelin, J.D., 2008. Eastern margin variability of the South Pacific Convergence Zone. Geophys. Res. Lett. 35, L16701. doi:10.1029/2008GL034298

Liu, J.B., Chen, F.H., Chen, J.H., Xia, D.S., Xu, Q.H., Wang, Z.L., Li, Y.C., 2011. Humid medieval warm period recorded by magnetic characteristics of sediments from Gonghai Lake, Shanxi, North China. Chinese Sci. Bull. 56, 2464–2474. doi:10.1007/s11434-011-4592-y

MacDonald, G., 1945. Petrography of the Wallis Islands. Bull. Geol. Soc. Am. 56, 861–872.

Maloney, A.E., Nelson, D.B., Richey, J.N., Prebble, M., Sear, D.A., Hassall, J.D., Langdon, P.G., Croudace, I.W., Zawadzki, A., Sachs, J.P., 2019. Reconstructing precipitation in the tropical South Pacific from dinosterol 2H/1H ratios in lake sediment. Geochim. Cosmochim. Acta 245, 190–206. doi:10.1016/j.gca.2018.10.028

Masson-Delmotte, V., Schulz, M., Abe-Ouchi, A., Beer, J., Ganopolski, A., González Rouco, J., Jansen, E., Lambeck, K., Luterbacher, J., Naish, T., Osborn, T., Otto-Bliesner, B., Quinn, T., Ramesh, Rojas, M., Shao, X., Timmermann, A., 2013. Information from Paleoclimate Archives, in: Stocker, T.F., Qin, D., Plattner, G.-K., Tignor, M., Allen, S., Boschung, J., Nauels, A., Xia, Y., Bex, V., Midgely, P.M. (Eds.), Climate Change 2013 - The Physical Science Basis. Contribution of Working Group 1 to the Fifth Assessment Report of the Intergovernnmental Panel on Climate Change. Cambridge University Press, Cambridge, United Kingdom and New York, NY, USA, pp. 383–464. doi:10.1017/CBO9781107415324.013

Matthews, A.J., 2012. A multiscale framework for the origin and variability of the South Pacific Convergence Zone. Q. J. R. Meteorol. Soc. 138, 1165–1178. doi:10.1002/qj.1870

Matthews, A.J., Hoskins, B.J., Slingo, J.M., Blackburn, M., 1996. Development of convection along the SPCZ within a Madden-Julian oscillation. Q. J. R. Meteorol. Soc. 122, 669–688. doi:10.1256/smsqj.53105

Maupin, C.R., Partin, J.W., Shen, C.-C., Quinn, T.M., Lin, K., Taylor, F.W., Banner, J.L., Thirumalai, K., Sinclair, D.J., 2014. Persistent decadal-scale rainfall variability in the tropical South Pacific Convergence Zone through the past six centuries. Clim. Past 10, 1319–1332. doi:10.5194/cp-10-1319-2014

Medina-Elizalde, M., Burns, S.J., Lea, D.W., Asmerom, Y., von Gunten, L., Polyak, V., Vuille, M., Karmalkar, A., 2010. High resolution stalagmite climate record from the Yucatán Peninsula spanning the Maya terminal classic period. Earth Planet. Sci. Lett. 298, 255–262. doi:10.1016/j.epsl.2010.08.016

Meisch, C., Mary-Sasal, N.J., Colin, J., Wouters, K., 2007. Freshwater Ostracoda (Crustacea) collected from the islands of Futuna and Wallis, Pacific Ocean, with a check-list of the non-marine Ostracoda of the Pacific Islands. Bull. Soc. Nat. luxemb. 108, 89–103.

Meyer, J.-Y., 2017. Guide des plantes de Wallis et Futuna. Éditions Au Vent des Îles, Papeete.

Metcalfe, S.E., Jones, M.D., Davies, S.J., Noren, A., MacKenzie, A., 2010. Climate variability over the last two millennia in the North American Monsoon region, recorded in laminated lake sediments from Laguna de Juanacatlán, Mexico. The Holocene 20, 1195–1206. doi:10.1177/0959683610371994

Nelson, D.B., Sachs, J.P., 2016. Galápagos hydroclimate of the Common Era from paired microalgal and mangrove biomarker 2H/1H values. Proc. Natl. Acad. Sci. U. S. A. 113, 3476–3481. doi:10.1073/pnas.1516271113

Nelson, D.B., Sachs, J.P., 2014. The influence of salinity on D/H fractionation in dinosterol and brassicasterol from globally distributed saline and hypersaline lakes. Geochim. Cosmochim. Acta 133, 325–339. doi:10.1016/j.gca.2014.03.007

Nelson, D.B., Sachs, J.P., 2013. Concurrent purification of sterols, triterpenols and alkenones from sediments for hydrogen isotope analysis using high performance liquid chromatography. Org. Geochem. 64, 19–28. doi:10.1016/j.orggeochem.2013.09.005

NOAA, 2021. Cold and Warm Episodes by Season [WWW Document]. (National Ocean. Atmos. Adm. URL https://origin.cpc.ncep.noaa.gov/products/analysis_monitoring/ensostuff/ONI_v5.php (accessed 10.11.21)

Ourbak, T., Corrège, T., Malaizé, B., Le Cornec, F., Charlier, K., Peypouquet, J.P., 2006. ENSO and interdecadal climate variability over the last century documented by geochemical records of two coral cores from the South West Pacific. Adv. Geosci. 6, 23–27. doi:10.5194/adgeo-6-23-2006

Papazian, M., Dumont, H.J., Mary-Sasal, N.J., 2007. The Odonata of the Pacific Ocean islands of Wallis and Futuna, with special reference to speciation in *Ischnura aurora* (Brauer). Odonatologica 36, 53–62.

Parkes, A., 1994. Holocene environments and vegetational change on four Polynesian islands. University of Hull.

Partin, J.W., Quinn, T.M., Shen, C.-C., Emile-Geay, J., Taylor, F.W., Maupin, C.R., Lin, K., Jackson, C.S., Banner, J.L., Sinclair, D.J., Huh, C.-A., 2013. Multidecadal rainfall variability in South Pacific Convergence Zone as revealed by stalagmite geochemistry. Geology 41, 1143–1146. doi:10.1130/G34718.1

Pierce, A.D., 2019. ncdf4: Interface to Unidata netCDF (Version 4 or Earlier) Format Data Files. R package version 1.17.

Plummer, C.T., Curran, M.A.J., Ommen, T.D. Van, Rasmussen, S.O., Moy, A.D., Vance, T.R., Clausen, H.B., Vinther, B.M., Mayewski, P.A., 2012. An independently dated 2000-yr volcanic record from Law Dome,

East Antarctica, including a new perspective on the dating of the 1450s CE eruption of Kuwae, Vanuatu. Climate of the Past 8, 1929–1940. doi:10.5194/cp-8-1929-2012

Polissar, P.J., D'Andrea, W.J., 2014. Uncertainty in paleohydrologic reconstructions from molecular δD values. Geochim. Cosmochim. Acta 129, 146–156. doi:10.1016/j.gca.2013.12.021

Price, R.C., Maillet, P., McDougall, I., Dupont, J., 1991. The geochemistry of basalts from the Wallis Islands, northern Melanesian Borderland: Evidence for a lithospheric origin for Samoan-type basaltic magmas? J. Volcanol. Geotherm. Res. 45, 267–288. doi:10.1016/0377-0273(91)90063-6

R Core Team, 2021. R: A Language and Environment for Statistical Computing.

Raos, A.M., Crawford, A.J., 2004. Basalts from the Efate Island Group, central section of the Vanuatu arc, SW Pacific: geochemistry and petrogenesis. J. Volcanol. Geotherm. Res. 134, 35–56. doi:10.1016/j.jvolgeores.2004.12.004

Rayner, N.A., Parker, D.E., Horton, E.B., Folland, C.K., Alexander, L. V., Rowell, D.P., Kent, E.C., Kaplan, A., 2003. Global analyses of sea surface temperature, sea ice, and night marine air temperature since the late nineteenth century. J. Geophys. Res. Atmos. 108. doi:10.1029/2002jd002670

Richey, J.N., Sachs, J.P., 2016. Precipitation changes in the western tropical Pacific over the past millennium. Geology 44, 671–674. doi:10.1130/G37822.1

Rodysill, J.R., Russell, J.M., Bijaksana, S., Brown, E.T., Safiuddin, L.O., Eggermont, H., 2012. A paleolimnological record of rainfall and drought from East Java, Indonesia during the last 1,400 years. J. Paleolimnol. 47, 125–139. doi:10.1007/s10933-011-9564-3

Rouwet, D., Christenson, B., Tassi, F., Vandemeulebrouck, J., 2015. Volcanic Lakes, Advances in Volcanology, Advances in Volcanology. Springer-Verlag, Berlin Heidelberg. doi:10.1007/978-3-642-36833-2_1

RStudio_Team, 2021. RStudio: Integrated Development Environment for R.

Rull, V., 2021. Contributions of paleoecology to Easter Island's prehistory: a thorough review. Quat. Sci. Rev. 252, 106751. doi:10.31223/OSF.IO/NF297

Saccocia, P.J., Seewald, J.S., Shanks, W.C., 1998. Hydrogen and oxygen isotope fractionation between brucite and aqueous NaCl solutions from 250 to 450°C. Geochim. Cosmochim. Acta 62, 485–492. doi:10.1016/S0016-7037(97)00346-3

Sachs, J.P., Blois, J.L., McGee, T., Wolhowe, M.D., Haberle, S.G., Clark, G., Atahan, P., 2018. Southward shift of the Pacific ITCZ during the Holocene. Paleoceanogr. Paleoclimatology 33, 1–13. doi:10.1029/2018PA003469

Sachs, J.P., Kawka, O.E., 2015. The influence of growth rate on 2H/1H fractionation in continuous cultures of the coccolithophorid *Emiliania huxleyi* and the diatom *Thalassiosira pseudonana*. PLoS One 10, e0141643. doi:10.1371/journal.pone.0141643

Sachs, J.P., Maloney, A.E., Gregersen, J., 2017. Effect of light on 2H/1H fractionation in lipids from continuous cultures of the diatom *Thalassiosira pseudonana*. Geochim. Cosmochim. Acta 209, 204–215. doi:10.1016/j.gca.2017.04.008

Sachs, J.P., Mügler, I., Sachse, D., Prebble, M., Wolhowe, M., 2021. Last millennium hydroclimate in the central equatorial North Pacific (5°N, 160°W). Quat. Sci. Rev. 259, 106906. doi:10.1016/j.quascirev.2021.106906

Sachs, J.P., Schwab, V.F., 2011. Hydrogen isotopes in dinosterol from the Chesapeake Bay estuary. Geochim. Cosmochim. Acta 75, 444–459. doi:10.1016/j.gca.2010.10.013

Sachse, D., Billault, I., Bowen, G.J., Chikaraishi, Y., Dawson, T.E., Feakins, S.J., Freeman, K.H., Magill, C.R., McInerney, F.A., van der Meer, M.T.J., Polissar, P.J., Robins, R.J., Sachs, J.P., Schmidt, H.-L., Sessions, A.L., White, J.W., West, J.B., Kahmen, A., 2012. Molecular paleohydrology: Interpreting the hydrogen-isotopic

composition of lipid biomarkers from photosynthesizing organisms. Annu. Rev. Earth Planet. Sci. 40, 221–249. doi:10.1146/annurev-earth-042711-105535

Salinger, M.J., McGree, S., Beucher, F., Power, S.B., Delage, F., 2014. A new index for variations in the position of the South Pacific convergence zone 1910/11-2011/2012. Clim. Dyn. 43, 881–892. doi:10.1007/s00382-013-2035-y

Sand, C., 2000. La datation du premier peuplement de Wallis et Futuna: contribution à la définition de la chronologie Lapita en Polynésie occidentale. J. Soc. Ocean. 111, 165–172. doi:10.3406/jso.2000.2132

Schabetsberger, R., Drozdowski, G., Rott, E., Lenzenweger, R., Jersabek, C.D., Fiers, F., Traunspurger, W., Reiff, N., Stoch, F., Kotov, A. a., Martens, K., Schatz, H., Kaiser, R., 2009. Losing the bounty? Investigating species richness in isolated freshwater ecosystems of Oceania. Pacific Sci. 63, 153–179. doi:10.2984/049.063.0201

Schabetsberger, R., Jersabek, C.D., Levkov, Z., Ehrenfellner, B., Enoka, L.F., Faiilagi, S.A., 2021. Limnological characterization of three tropical crater lakes in the archipelago of Samoa (Lanoto'o, Olomaga, Mataulano). Pacific Sci. 75, 163–174. doi:10.2984/75.1.8

Schanze, J.J., Schmitt, R.W., Yu, L.L., 2010. The global oceanic freshwater cycle: A state-of-the-art quantification. J. Mar. Res. 68, 569–595. doi:10.1357/002224010794657164

Schneider, U., Becker, A., Ziese, M., Rudolf, B., 2018. Global Precipitation Analysis Products of the GPCC. Glob. Precip. Climatol. Cent. 1–14.

Schwab, V.F., Garcin, Y., Sachse, D., Todou, G., Séné, O., Onana, J.M., Achoundong, G., Gleixner, G., 2015. Dinosterol δD values in stratified tropical lakes (Cameroon) are affected by eutrophication. Org. Geochem. 88, 35–49. doi:10.1016/j.orggeochem.2015.08.003

Sear, D.A., Allen, M.S., Hassall, J.D., Maloney, A.E., Langdon, P.G., Morrison, A.E., Henderson, A.C.G., Mackay, H., Croudace, I.W., Clarke, C., Sachs, J.P., Macdonald, G., Chiverrell, R.C., Leng, M.J., Cisneros-Dozal, L.M., Fonville, T., 2020. Human settlement of East Polynesia earlier, incremental, and coincident with prolonged South Pacific drought. Proc. Natl. Acad. Sci. 117, 8813–8819. doi:10.1073/pnas.1920975117

Sémah, A.-M., Wirrmann, D., 2006. Mission Vanuatu - du 9 septembre au 2 décembre 2005 (Rapport de missions No. 67). Sci. la Terre Géologie-Géophysique, IRD.

Sessions, A.L., Burgoyne, T.W., Schimmelmann, A., Hayes, J.M., 1999. Fractionation of hydrogen isotopes in lipid biosynthesis. Org. Geochem. 30, 1193–1200. doi:10.1016/S0146-6380(99)00094-7

Shaw, B., Coxe, S., Kewibu, V., Haro, J., Hull, E., Hawkins, S., 2020. 2500-year cultural sequence in the Massim region of eastern Papua New Guinea reflects adaptive strategies to small islands and changing climate regimes since Lapita settlement. Holocene 30, 1075–1090. doi:10.1177/0959683620908641

Shuler, C.K., Dulai, H., DeWees, R., Kirs, M., Glenn, C.R., El-Kadi, A.I., 2019. Isotopes, microbes, and turbidity: A multi-tracer approach to understanding recharge dynamics and groundwater contamination in a basaltic island aquifer. Groundw. Monit. Remediat. 39, 20–35. doi:10.1111/gwmr.12299

Sichrowsky, U., Schabetsberger, R., Sonntag, B., Stoyneva, M., Maloney, A.E., Nelson, D.B., Richey, J.N., Sachs, J.P., 2014. Limnological characterization of volcanic crater lakes on Uvea Island (Wallis and Futuna, South Pacific). Pacific Sci. 68, 333–343. doi:10.2984/68.3.3

Smittenberg, R.H., Saenger, C., Dawson, M.N., Sachs, J.P., 2011. Compound-specific D/H ratios of the marine lakes of Palau as proxies for West Pacific Warm Pool hydrologic variability. Quat. Sci. Rev. 30, 921–933. doi:10.1016/j.quascirev.2011.01.012

St. John, H., Smith, A.C., 1971. The vascular plants of the Horne and Wallis Islands. Pacific Sci. 25, 313–348.

Stearns, H.T., 1945. Geology of the Wallis Islands. Bull. Geol. Soc. Am. 56, 849–860. doi:10.1130/0016-7606(1945)56[849:GOTWI]2.0.CO;2

Stevens, K., 2018. Wasting coconuts? Consumption versus commerce in colonial Wallis and Futuna. J. Pac. Hist. 53, 478–501. doi:10.1080/00223344.2018.1542294

Takahashi, K., Battisti, D.S., 2007a. Processes controlling the mean tropical Pacific precipitation pattern. Part II: The SPCZ and the southeast Pacific dry zone. J. Clim. 20, 5696–5706. doi:10.1175/2007JCLI1656.1

Takahashi, K., Battisti, D.S., 2007b. Processes controlling the mean tropical Pacific precipitation pattern. Part I: The Andes and the eastern Pacific ITCZ. J. Clim. 20, 3434–3451. doi:10.1175/JCLI4198.1

Tangri, N., Dunbar, R.B., Linsley, B.K., Mucciarone, D.M., 2018. ENSO's shrinking 20th Century footprint revealed in a half-millennium coral core from the South Pacific Convergence Zone. Paleoceanogr. Paleoclimatology 33, 1136–1150. doi:10.1029/2017PA003310

Thibault, J.-C., Cibois, A., Meyer, J.-Y., 2015. Birds of Uvea (Wallis), Futuna and Alofi islands (South-West Pacific): an update. Notornis 62, 30–37.

Tierney, J.E., Oppo, D.W., Rosenthal, Y., Russell, J.M., Linsley, B.K., 2010. Coordinated hydrological regimes in the Indo-Pacific region during the past two millennia. Paleoceanography 25, 1–7. doi:10.1029/2009PA001871

Toner, J.D., Catling, D.C., 2020. A carbonate-rich lake solution to the phosphate problem of the origin of life. Proc. Natl. Acad. Sci. 117, 883–888. doi:10.1073/pnas.1916109117

Toomey, M.R., Donnelly, J.P., Tierney, J.E., 2016. South Pacific hydrologic and cyclone variability during the last 3000 years. Paleoceanography 31, 491–504. doi:10.1002/2015PA002870

United Nations, 2019. World Population Prospects 2019 [WWW Document]. Dep. Econ. Soc. Aff. Popul. Div. URL https://population.un.org/wpp/DataQuery/ (accessed 3.10.21).

van der Wiel, K., Matthews, A.J., Joshi, M.M., Stevens, D.P., 2016. Why the South Pacific Convergence Zone is diagonal. Clim. Dyn. 46, 1683–1698. doi:10.1007/s00382-015-2668-0

van der Wiel, K., Matthews, A.J., Stevens, D.P., Joshi, M.M., 2015. A dynamical framework for the origin of the diagonal South Pacific and South Atlantic Convergence Zones. Q. J. R. Meteorol. Soc. 141, 1997–2010. doi:10.1002/qj.2508

Vincent, E.M., Lengaigne, M., Menkes, C.E., Jourdain, N.C., Marchesiello, P., Madec, G., 2011. Interannual variability of the South Pacific Convergence Zone and implications for tropical cyclone genesis. Clim. Dyn. 36, 1881–1896. doi:10.1007/s00382-009-0716-3

Volkman, J.K., 2005. Sterols and other triterpenoids: source specificity and evolution of biosynthetic pathways. Org. Geochem. 36, 139–159. doi:10.1016/j.orggeochem.2004.06.013

Volkman, J.K., Barrett, S.M., Blackburn, S.I., Mansour, M.P., Sikes, E.L., Gelin, F., 1998. Microalgal biomarkers: A review of recent research developments. Org. Geochem. 29, 1163–1179. doi:10.1016/S0146-6380(98)00062-X

Volkman, J.K., Barrett, S.M., Dunstan, G.A., Jeffrey, S.W., 1993. Geochemical significance of the occurrence of dinosterol and other 4-methyl sterols in a marine diatom. Org. Geochem. 20, 7–15. doi:10.1016/0146-6380(93)90076-N

Wang, J., Yang, B., Ljungqvist, F.C., Luterbacher, J., Osborn, T.J., Briffa, K.R., Zorita, E., 2017. Internal and external forcing of multidecadal Atlantic climate variability over the past 1,200 years. Nat. Geosci. 10, 512–517. doi:10.1038/ngeo2962

Widlansky, M.J., Webster, P.J., Hoyos, C.D., 2011. On the location and orientation of the South Pacific Convergence Zone. Clim. Dyn. 36, 561–578. doi:10.1007/s00382-010-0871-6

Wyman, D.A., Conroy, J.L., Osburn, M.R., Atwood, A.R., 2021. Coeval drying across the central tropical Pacific over the last millennium. Paleoceanogr. Paleoclimatology 36, 1–15. doi:10.1029/2021PA004311

Yu, L., Jin, X., Weller, R.A., 2008. Multidecade Global Flux Datasets from the Objectively Analyzed Air-sea Fluxes (OAFlux) Project: Latent and sensible heat fluxes, ocean evaporation, and related surface meteorological variables. OAFlux Proj. Tech. Rep. OA-2008-01 Woods Hole Oceanogr. Inst. doi:10.1007/s00382-011-1115-0

Zhang, R., Sutton, R., Danabasoglu, G., Kwon, Y.O., Marsh, R., Yeager, S.G., Amrhein, D.E., Little, C.M., 2019. A review of the role of the Atlantic meridional overturning circulation in Atlantic multidecadal variability and associated climate impacts. Rev. Geophys. 57, 316–375. doi:10.1029/2019RG000644

Zhang, X., Gillespie, A.L., Sessions, A.L., 2009. Large D/H variations in bacterial lipids reflect central metabolic pathways. Proc. Natl. Acad. Sci. U. S. A. 106, 12580–6. doi:10.1073/pnas.0903030106

Zhang, Z., Sachs, J.P., 2007. Hydrogen isotope fractionation in freshwater algae: I. Variations among lipids and species. Org. Geochem. 38, 582–608. doi:10.1016/j.orggeochem.2006.12.004

Zhang, Z., Sachs, J.P., Marchetti, A., 2009. Hydrogen isotope fractionation in freshwater and marine algae: II. Temperature and nitrogen limited growth rate effects. Org. Geochem. 40, 428–439. doi:10.1016/j.orggeochem.2008.11.002

Appendix A

Appendix B (Separate Excel file via https://doi.org/10.1016/j.quascirev.2022.107421 and/or via PANGEA repository https://www.pangaea.de/)

Section A.1. Sedimentary microfossil survey

A preliminary assessment of diatom and chironomid presence was performed using sediment recovered along the entirety of the core barrel edge from LALOUC13 and LATVKUC4 during core splitting. Diatom sample preparation followed (Battarbee et al., 2001) and chironomid sample preparation followed (Walker, 2001). The concentration of chironomid head-capsules was very low in both Lac Lalolalo and Lanutavake yielding less than 10 head-capsules per gram of dry sediment. Diatom concentration was low (c. 10%) in Lac Lalolalo sediments and dominant taxa were mainly Nitzschioid taxa (tentatively identified as *Nitzschia frustulum/perminuta* and *Nitzschia palustris*) as well as some large periphytic taxa such as *Pinnularia borealis*. In Lac Lanutavake the diatom concentration was low-moderate (c. 20%), and the predominantly periphytic/benthic identified taxa belong to the *Gomphonema* group (tentatively identified as *Gomphonema gracile* and *Gomphoneis cf. minuta*). Given the low concentrations of microfossils in these sediments, they were deemed unsuitable for stable isotope analysis on chironomids and diatoms. Both lakes had high amounts of dark orange/brown minerals that obfuscated the diatoms.

Table A.1. Mean gridded GPCPv2.3 precipitation rates (mm d^{-1}) (Adler et al., 2018) and estimated precipitation errors (σ) (Adler et al., 2012) for the 1979–2016 period and during specified intervals at lake sites. El Niño (La Niña) conditions are taken as periods when the Oceanic Niño Index, derived from sea surface temperature anomalies in the Niño 3.4 region, was above (below) 0.5 °C (www.esrl.noaa.gov/psd/data/climateindices/list)

Island	Mean	σ	SD	DJF	SD	JJA	SD	[DJF−JJA]	El Niño	SD	La Niña	SD	[Niña−Niño]
ʻUvea, Wallis	6.0	1.4	3.7	8.6	4.3	3.4	1.9	5.2	5.9	3.5	6.7	4.3	0.8
ʻUpolu, Samoa	5.6	1.4	3.4	8.4	3.7	2.8	1.3	5.6	5.5	3.1	6.2	3.9	0.7
Efate, Vanuatu	4.8	0.9	3.1	6.5	3.5	3.0	1.7	3.5	4.1	2.8	6.1	3.5	2.0

Table A.2. Vascular plants surrounding Lake Lalolalo shoreline. N= Native; A = Alien

Family	**Genus species**	**Origin**
Acanthaceae	*Ruellia prostrata*	A
Apocynaceae	*Alyxia* sp.	N
Apocynaceae	*Cerbera manghas*	N
Asclepiadaceae	*Hoya australis*	N
Aspleniaceae	*Asplenium nidus*	N
Aspleniaceae	*Asplenium polyodon*	N
Blechnaceae	*Stenochlaena palustris*	N
Calophyllaceae	*Calophyllum inophyllum*	N
Capparaceae	*Capparis spinosa* subsp. *cordifolia*	N
Combretaceae	*Terminalia catappa*	A
Davalliaceae	*Davallia solida*	N
Davalliaceae	*Nephrolepis hirsutula*	N
Ebenaceae	*Diospyros samoensis*	N
Elaeocarpaceae	*Elaeocarpus angustifolius*	N
Euphorbiaceae	*Acalypha grandis*	N
Euphorbiaceae	*Homalanthus nutans*	N
Euphorbiaceae	*Macaranga harveyana*	N
Lecythidaceae	*Barringtonia asiatica*	N
Leguminosae	*Adenanthera pavonina*	A
Leguminosae	*Entada phaseoloides*	N
Leguminosae	*Inocarpus fagifer*	N
Leguminosae	*Mucuna gigantea*	N
Loganiaceae	*Geniostoma* cf. *rupestre*	N
Malvaceae	*Talipariti tiliaceum*	N
Melastomataceae	*Clidemia hirta*	A
Meliaceae	*Azadirachta indica*	A
Meliaceae	*Dysoxylum mollissimum*	N
Moraceae	*Ficus obliqua*	N
Myrtaceae	*Syzygium clusiifolium*	N
Orchidaceae	*Bulbophyllum* sp.	N
Pandanaceae	*Pandanus tectorius*	N
Passifloraceae	*Passiflora foetida*	A
Polypodiaceae	*Microsorum* cf. *grossum*	N
Polypodiaceae	*Pyrrosia lanceolata*	N
Psilotaceae	*Psilotum nudum*	N
Pteridaceae	*Antrophyum plantagineum*	N
Rubiaceae	*Aidia cochinchinensis*	N
Rubiaceae	*Morinda citrifolia*	A
Rutaceae	*Micromelum minutum*	N
Sapindaceae	*Sapindus* cf. *saponaria*	N
Verbenaceae	*Premna serratifolia*	N
Verbenaceae	*Stachytarpheta* cf. *urticifolia*	A
Zingiberaceae	*Alpinia zerumbet*	A

Table A.3. Sediment collection and sampling details.

Site Name	Latitude	Longitude	Core ID	Collection date	Sample technique*	Field-sectioned material	Total sediment core length	Deepest ^{14}C age control	Deepest dinosterol sample
	°	°		YYMMDD		cm	cm	cm	cm
Lac Lalolalo, 'Uvea, Wallis	−13.30108	183.765917	LALOUC13	110516	UC	97	161.5	152.25	152.5–153.5
Lac Lalolalo, 'Uvea, Wallis	−13.30048	183.766000	LALOUC14	110517	UC	40	168	156.5	156–157
Lac Lalolalo, 'Uvea, Wallis	−13.30168	183.768083	LALOUC22	110519	UC	16	38	13.5	12–13
Lac Lalolalo, 'Uvea, Wallis	−13.30168	183.768039	LALOUC24	110519	UC	27	27	8	10–11
Lac Lanutavake, 'Uvea, Wallis	−13.32118	183.786033	LATVKUC1	110518	UC	18	143	106.3	138–139
Lac Lanutavake, 'Uvea, Wallis	−13.32115	183.786133	LATVKUC4	110519	UC	38.5	77.5	67.5	72.5–73.5
Lake Lanoto'o, 'Upolu, Samoa[1]	−13.91088	188.172600	LAN14 U2 + L1-1	140930	GC + L	0	302	299.5	83–84
Emaotul Lake, Efate, Vanuatu[1]	−17.72989	168.415462	VAN[2]	150910	GC + L	0	360	338.3	349.9–350.9

[1]Sear et al. 2020, Maloney et al. 2019

[2]Cores/sections: G5, G9, L1, L1A, L2, L2A, L3, L3A. Coretop sample includes G7 (0–2 cm), G5 (0–2 cm), and a 0–1cm section collected in 1995 (Maloney et al. 2019)

*UC = Universal Corer, GC = UWITEC gravity core, L = Livingston

Table A.4. ^{14}C dates from 'Uvea terrestrial macrofossils. Depths from LATVKUC1 were adjusted to match a combined age model based on magnetic susceptibility trace (see **Fig. A.5**), see **Table B.1** for age models using these and previously published ^{210}Pb age control points.

Lab Sample ID	Core	Sampled interval (cm)	Core depth (cm) [adjusted depth]	% modern carbon	±	^{14}C age	Error (1 σ)
Lac Lanutavake							
D-AMS 022790*	LATVKUC1	14 – 15	14.5 [18.18]	96.9	0.52	255	43
D-AMS 022791*	LATVKUC1	36 – 37	36.5 [44.77]	92.3	0.35	640	30
D-AMS 017995	LATVKUC1	88.5	88.5 [91.05]	85.2	0.24	1288	23
D-AMS 022792	LATVKUC1	102 – 103	102.5 [105.09]	82.8	0.33	1514	32
D-AMS 017996	LATVKUC1	133	133 [136.81]	81.2	0.25	1672	25
CAMS 153012*	LATVKUC4	2 – 4.5	3.25	142.4	0.51	>Modern	
D-AMS 006998*	LATVKUC4	26	26	94.9	0.25	420	21
D-AMS 006999	LATVKUC4	38 – 38.5	38.25	92.3	0.28	644	24
CAMS 153013	LATVKUC4	44.5	44.5	89.3	0.32	905	30
D-AMS 009275	LATVKUC4	67.5	67.5	84.5	0.24	1355	23
Lac Lalolalo							
CAMS 153008	LALOUC13	36.5	36.5	96.7	0.35	265	30
D-AMS 022795	LALOUC13	46 – 47	46.5	94.4	0.87	464	74
D-AMS 022796	LALOUC13	56 – 57	56.5	94.8	0.54	426	46
D-AMS 022797	LALOUC13	66 – 67	66.5	95.4	0.36	379	30
D-AMS 022798	LALOUC13	76 – 77	76.5	92.4	0.40	634	35
D-AMS 017993	LALOUC13	104	104	89.2	0.41	920	37
D-AMS 022799	LALOUC13	127 – 128	127.5	83.5	0.47	1450	45
CAMS 153009	LALOUC13	155	155	82.9	0.30	1505	30
D-AMS 026255	LALOUC14	15 – 16	15.5	95.0	0.36	414	30
D-AMS 022805	LALOUC14	18 – 19	18.5	95.3	0.56	391	47
D-AMS 022806	LALOUC14	27 – 28	27.5	81.1	0.35	1685	35
D-AMS 022807	LALOUC14	33 – 34	33.5	78.1	0.48	1986	49
D-AMS 017997	LALOUC14	53	53	85.0	0.29	1309	27
D-AMS 026256	LALOUC14	72.5	72.5	77.4	0.42	2060	44
D-AMS 026257	LALOUC14	112	112	79.8	0.32	1817	32
D-AMS 017998	LALOUC14	125	125	79.4	0.21	1856	21
D-AMS 026258	LALOUC14	161 – 162	161.5	71.6	0.34	2683	38
D-AMS 009276*	LALOUC22	1 – 2	1.5	106.5	0.26	>Modern	
D-AMS 009277*	LALOUC22	13 – 14	13.5	99.3	0.24	56	19
D-AMS 026259	LALOUC24	0 – 1	0.5	124.3	0.38	>Modern	

*Previously published in Maloney et al. (2019)

Table A.5. Mean $\delta^2H_{dinosterol}$ values and corresponding precipitation values for modern, LIA, and MCA, and total core periods with standard deviations and mean precipitation error.

Site	Modern: 1850–present						LIA: 1450–1850						MCA: 950–1250						Total core mean					
	mean	SD	mean	SD	error	n	mean	SD	mean	SD	error	n	mean	SD	mean	SD	error	n	mean	SD	mean	SD	error	n
	‰	‰	mm d^{-1}	mm d^{-1}	mm d^{-1}		‰	‰	mm d^{-1}	mm d^{-1}	mm d^{-1}		‰	‰	mm d^{-1}	mm d^{-1}	mm d^{-1}		‰	‰	mm d^{-1}	mm d^{-1}	mm d^{-1}	
Lac Lanutavake. ʻUvea	−288	5	6.3	0.4	2.2	12	−289	4	6.4	0.3	2.2	14	−283	4	6.0	0.2	2.1	5	−288	4	6.3	0.4	2.3	53
Lake Lanotoʻo, ʻUpolu	−281	5	5.7	0.4	2.1	4	−271	4	5.0	0.3	2.0	3	−268	11	4.7	0.3	2.0	3	−274	8	5.2	0.7	2.0	22
Lake Emaotul, Efate	−272	7	5.0	0.6	2.0	7	−271	6	4.9	0.5	2.0	11	−270	6	4.9	0.5	2.0	6	−276	10	5.4	0.9	2.1	41

Table A.6. Lac Lalolalo (ʻUvea) ions, metals, and (for reference) environmental field data from hand-held monitoring system submerged into a Nisken bottle or measured *in situ* down to 25 m (Maloney et al., 2019; Sichrowsky et al., 2014). All values are in mg L^{-1}, "nd" indicates not detected, "TR" indicates trace; some metals were not detected (Cd, Cu, Fe, Mo, Al, Pb) or not detected/trace at all depths (Cr, P, Zn, Ag). Titration data should be considered preliminary. Also shown are the mean Pacific seawater values (Nozaki, 1997) used to calculate relative % for main text **Fig. 3D-E**.

Depth (m)	Field data: Salinity	Temperature (°C)	pH *in situ*	pH Niskin	Titration (0.0245N H_2SO_4): pH lab	pH 8.3 1st end (mL)	pH 4.5 2nd end (mL)	sample (mL)	CO_3^{2-}	HCO_3^-
4	0.87	29.7	8.4	7.1	8.2	0	0.50	10		74
15	1.1	29.0	6.8	6.9	8.0	0	0.81	10		121
35	1.9	27.4		7.0	8.3	0	1.46	10		219
50	3.5	27.5		6.8	8.8	0.13	1.27	10	19	152
70	21.5	27.8		6.4	8.1	0	12.93	10		1933
80	31.5	27.5		6.5	8.5	5.14	9.35	5	1513	

Depth (m)	IC: F^-	Cl^-	NO_3^-	PO_4^{3-}	SO_4^{2-}	ICP-AES: As	B	Ba	Ca	K	Mg	Mn	Na	Ni	S	Se	Si
4	0.53	768	0.70	0.61	37.5	0.11	0.08	TR	15	7	32	0.09	251	0.03	15	nd	8
15	0.63	700	1.89	0.81	26.5	0.14	0.09	0.02	19	8	38	0.18	303	0.03	15	TR	7
35	0.79	1413	2.51	2.71	22.5	nd	nd	nd	29	19	64	TR	544	nd	16	nd	13
50	0.65	1228	0.70	3.60	19.2	nd	nd	nd	28	21	57	TR	467	nd	TR	nd	12
70	1.2	19292	8.22	17.30	21.6	TR	1.7	nd	74	174	731	TR	6071	TR	44	3.6	TR
80	36	29987	11.39	27.07	88.5	3.8	2.7	nd	353	294	1092	0.61	8995	0.97	194	TR	11
seawater	*1.22*	*19351*	*1.86*	*0.285*	*2713*		*4.5*		*412*	*399*	*1284*		*10784*				*1.8*

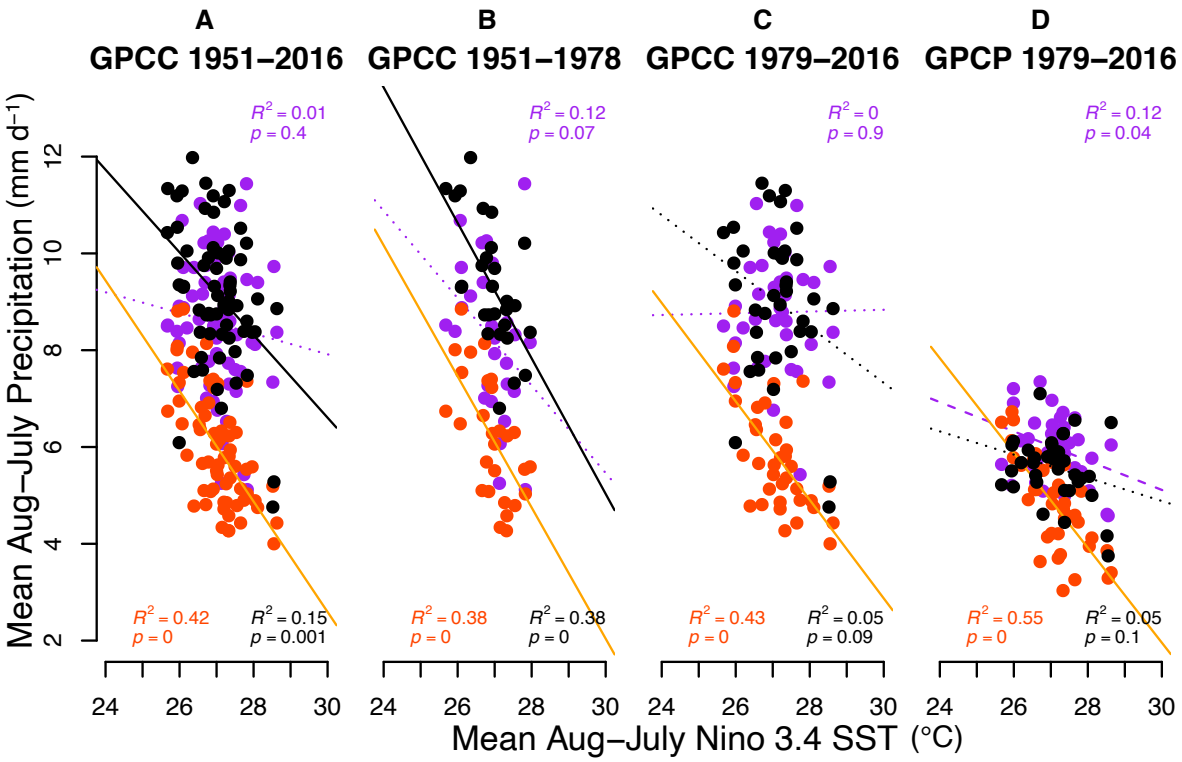

Figure A.1. Mean annual (August to July) GPCC gauge and GPCP satellite-gauge precipitation rates (both 2.5° x 2.5° grid) on ʻUvea (purple), ʻUpolu (black), and Efate (orange) versus Niño 3.4 region sea surface temperatures (SST). The 1951 – 2016 period (GPCC gauge data extends back to 1951 at ʻUvea) is shown in panel (A), GPCC is split into early (1951 – 1978) (B), and late (1979 – 2016) (C), to compare to the GPCP (1979 – 2016) satellite-gauge record (D). Precipitation rates on Efate are always well correlated with Nino3.4 SSTs, while precipitation rates on ʻUpolu are best correlated will Nino3.4 SSTs 1951 – 1978, and precipitation rates on ʻUvea are never well correlated with Niño 3.4 SSTs. Solid regression line indicates correlation significant below the p = 0.01 level, dashed lines indicates correlation significant below the p = 0.05 level, dotted lines indicates correlation not significant.

Figure A.2. Lake setting. Note the near-vertical bare cliffs of Lac Lalolalo compare to the more gradual sloping lake walls of Lac Lanutavake and Lac Lano. The more gradual sloping lake walls of the smaller lakes can also be seen on the topographic map (https://www.openstreetmap.org/#map=14/-13.2883/-176.2305&layers=C).

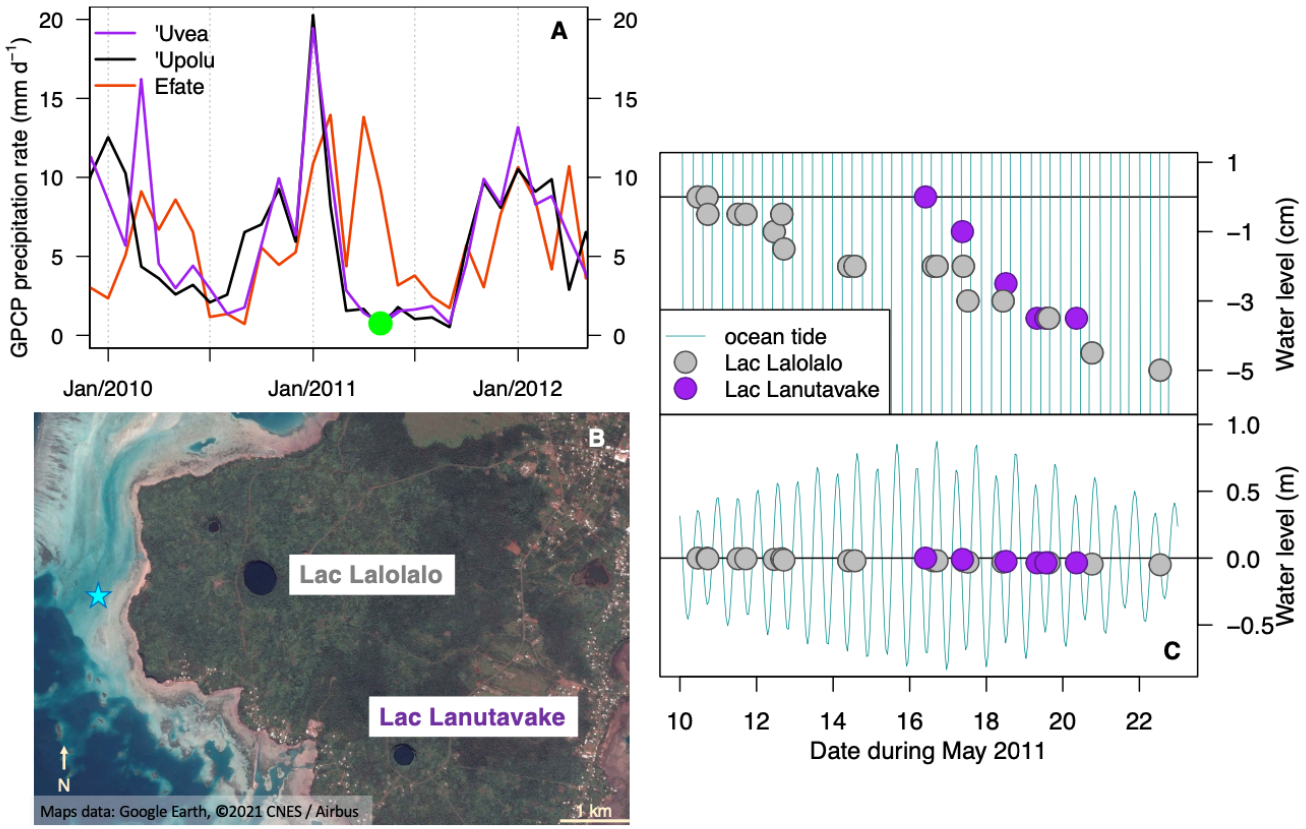

Figure A.3. Precipitation rates, ocean tidal cycle, and lake water levels during our visit. (A) Mean monthly gridded GPCP precipitation rates during our May 2011 visit to ʻUvea indicated by a green dot, a relatively drier part of the seasonal cycle. (B) Lake location compare to ocean tide location (–13.3056°, –176.2531° (blue star) from 136 m water depth (Egbert and Erofeeva, 2002), https://tpxows.azurewebsites.net/). (C) Lake water level readings (dots) compared to the ocean tidal cycle (thin blue line) indicates that there was no tidal influence on lake levels which slightly decreased during the length of observations (Lac Lalolalo's water level fell by ~5 cm over 12 days (gray dots) and Lac Lanutavake's water level fell by ~3.5 cm over 4 days (purple dots)) likely due to evaporative loss from the lake surface and/or reduction of the island's water table. Note the upper panel of (C) is on a centimeter scale to highlight the minor lake level changes and the lower panel is on a meter scale.

Figure A.4 Sediment core locations from Lac Lanutavake (top) and Lac Lalolalo (bottom).

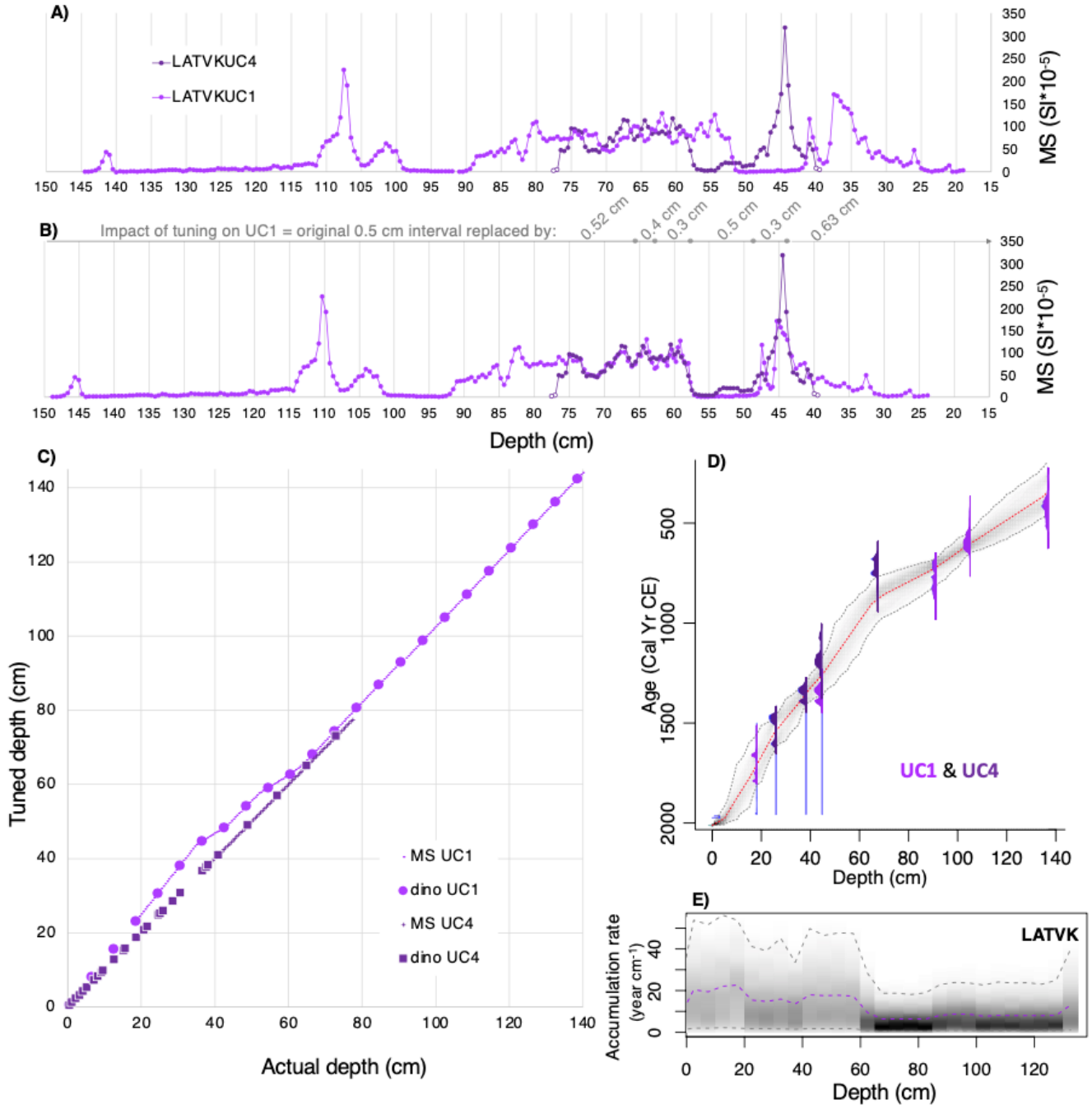

Figure A.5 The similarities between magnetic susceptibility (MS) responses in cores from Lac Lanutavake (A) were used to move both cores onto the same depth scale by changing the total width of each 0.5 cm interval (from 0.3 to 0.63 cm) (B) in UC1 to match UC4 which remained unchanged (C). ^{14}C and ^{210}Pb based BACON age models for Lac Lanutavake (tuned depths were used from UC1 to create a single age model), in all cases the top of the core was assumed to have an age equal to collection date (D). Panel E shows the accumulation rate of sediment in the combined age model.

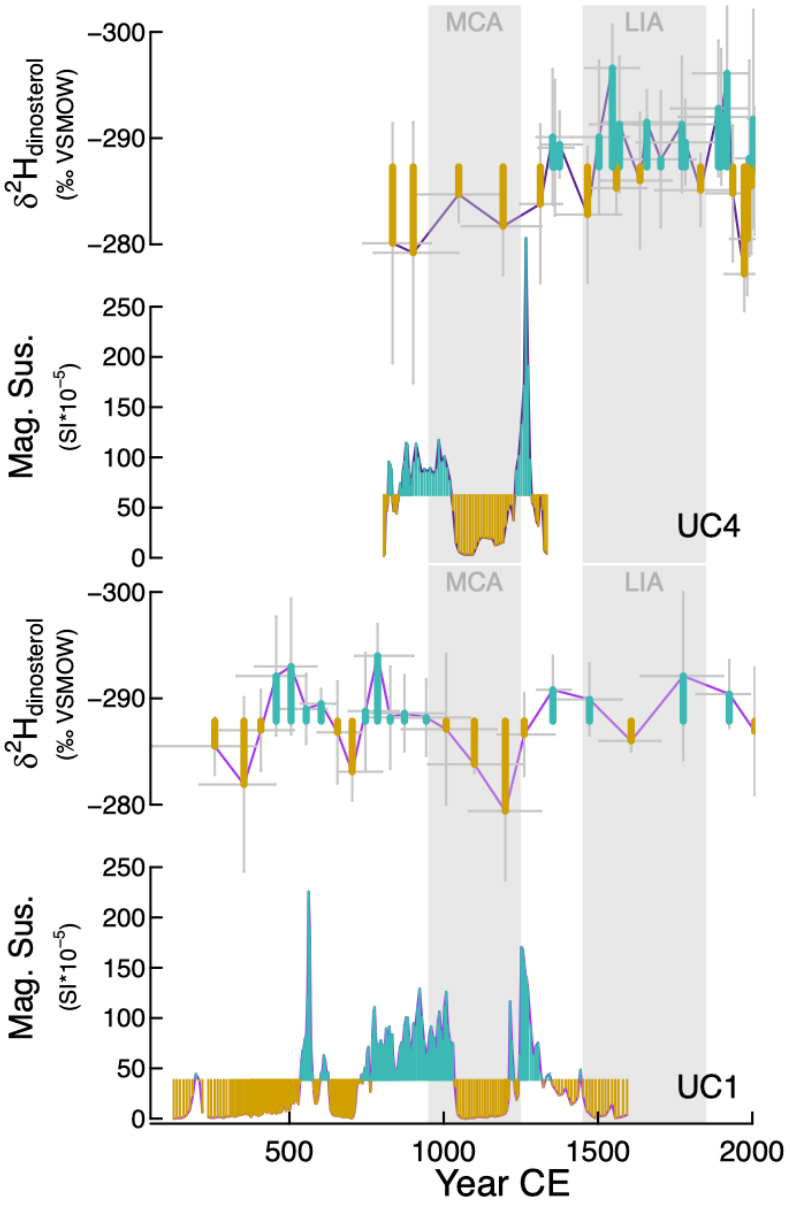

Figure A.6. Comparison between Lac Lanutavake (ʻUvea, Wallis et Futuna) $\delta^2H_{dinosterol}$ and magnetic susceptibility (Mag. Sus.) records from sediment cores UC1(bottom panels) and UC4 (top panels). Green segments indicate increased precipitation/less evaporation leading to relatively ^2H-depleted $\delta^2H_{dinosterol}$ values and high magnetic susceptibility signals from terrestrial runoff; brown segments indicate drier periods. Vertical shading represents the MCA and LIA, error bars indicate age model uncertainty (not shown for magnetic susceptibility records) and analytical uncertainty in $\delta^2H_{dinosterol}$ values. Note, magnetic susceptibility data for the uppermost portions of the cores is not available (these were sectioned in the field: top 18 cm at 1cm intervals for UC1 and the top 38.5 cm at 0.5 cm intervals for UC4).

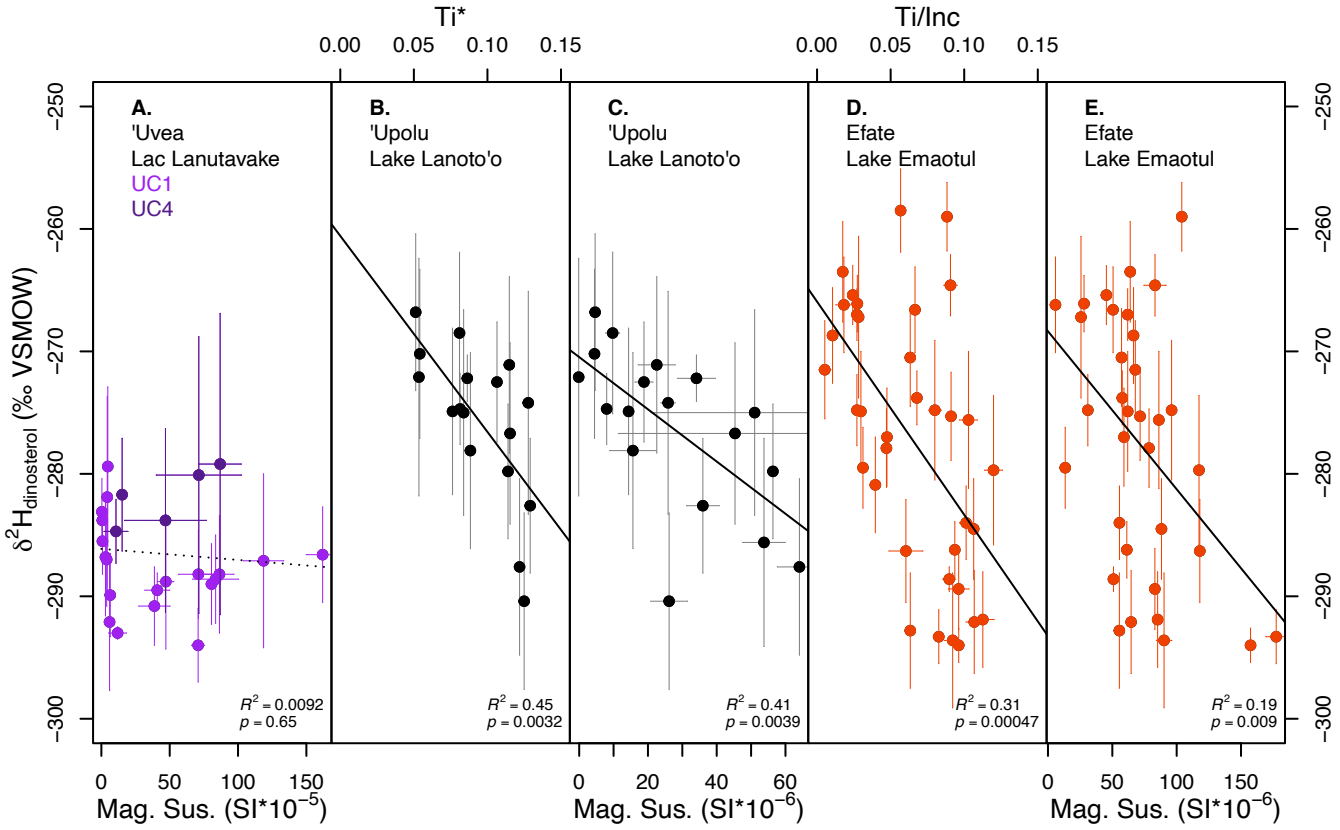

Figure A.7. $\delta^2H_{dinosterol}$ values versus runoff data from Lac Lanutavake ('Uvea, Wallis), Lake Lanoto'o ('Upolu, Samoa), and Lake Emaotul (Efate, Vanuatu). Magnetic susceptibility (Mag. Sus.) data is the average of two readings (the same 1cm interval as $\delta^2H_{dinosterol}$ and the interval immediately preceding), error bars indicate the difference between the two readings. The regression analysis for Lac Lanutavake (A) combines cores UC1 (20 points light purple) and UC4 (5 points dark purple) (note there is no magnetic susceptibility data from the upper 18 cm (UC1) and 38.5 cm (UC4) portions of these cores that were sectioned in the field). (B) Ti* data from Lake Lanoto'o is the average of 51 data points per cm in LAN14-U2, and 21 data points per cm in LAN14-L1-1, and (D) Ti/Inc from Lake Emoatul is the average of 50-51 data points per cm from L1, L1A, L2, L2A, L3, L3A and error bars for Ti* and Ti/Inc are the standard deviations of all data points in each interval. Lake Lanoto'o Ti* (B) and magnetic susceptibility (C) plots only include $\delta^2H_{dinosterol}$ values before and after runoff versus $\delta^2H_{dinosterol}$ values become anticorrelated due to exposed sediment at a lower lake level. In Lake Emaotul two exceptionally high magnetic susceptibility values (E) resulting from the Kuwae eruption data are not included. Solid regression lines indicates correlation significant below the p = 0.01 level, dotted line indicates correlation not significant.

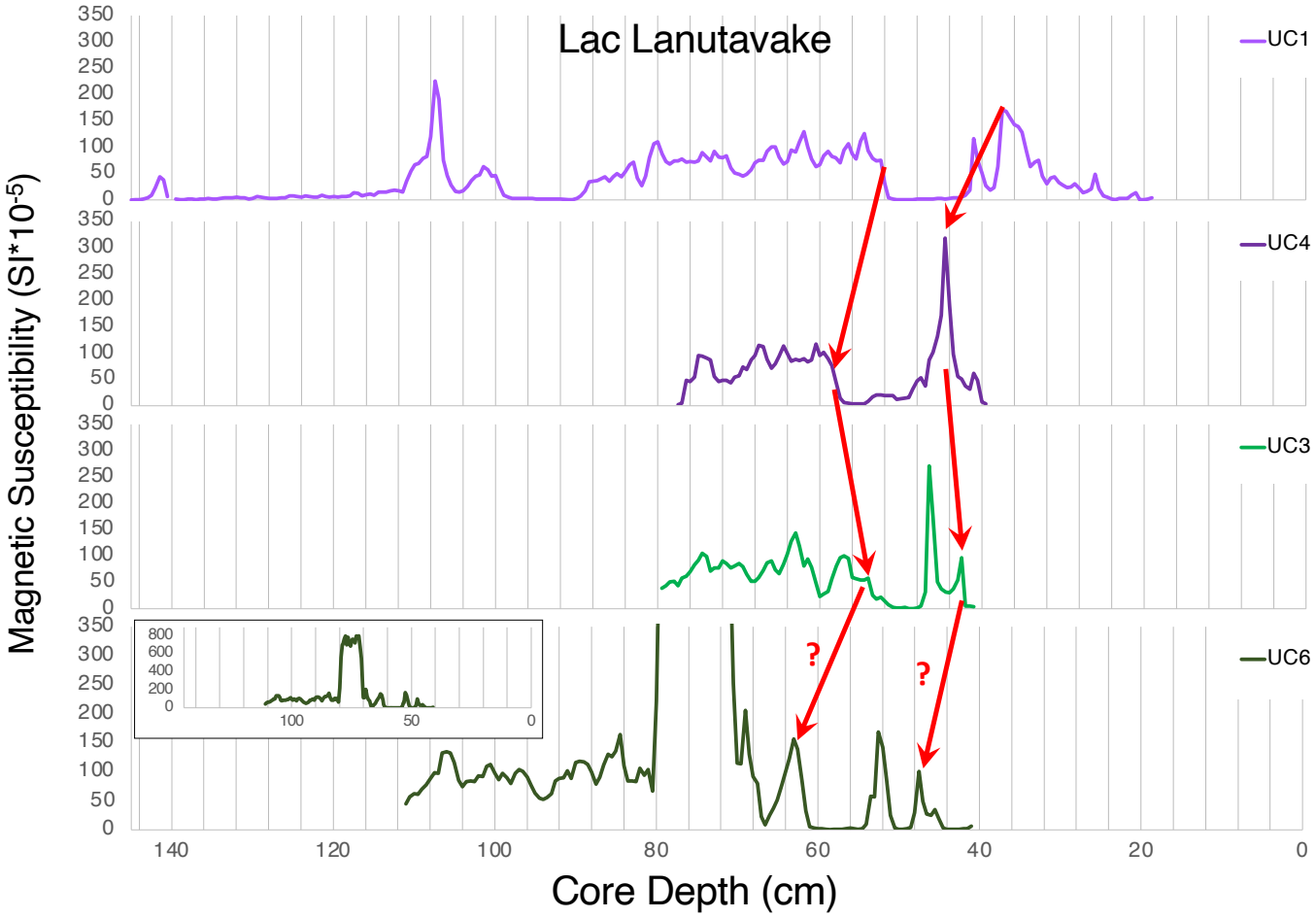

Figure A.8. Magnetic susceptibility signals from all cores taken from Lac Lanutavake (ʻUvea, Wallis et Futuna). UC1 and UC4 are same as main text **Figure 2**. UC6 is the sediment core taken close to the steepest cliffs on the northern side of the lake captures a large magnetic susceptibility event with signals >twice the size as those found in UC1, UC4 (and nearby UC3) which were located 20 to 34 m to the southwest of UC6. The large unreplicated event in UC6 might be the result of mass erosion of the northern cliff wall (and gradual settlement of suspended material throughout the rest of the lakebed). This suggests that magnetic susceptibility signals in Lac Lanutavake may only record erosion events after very intense precipitation.

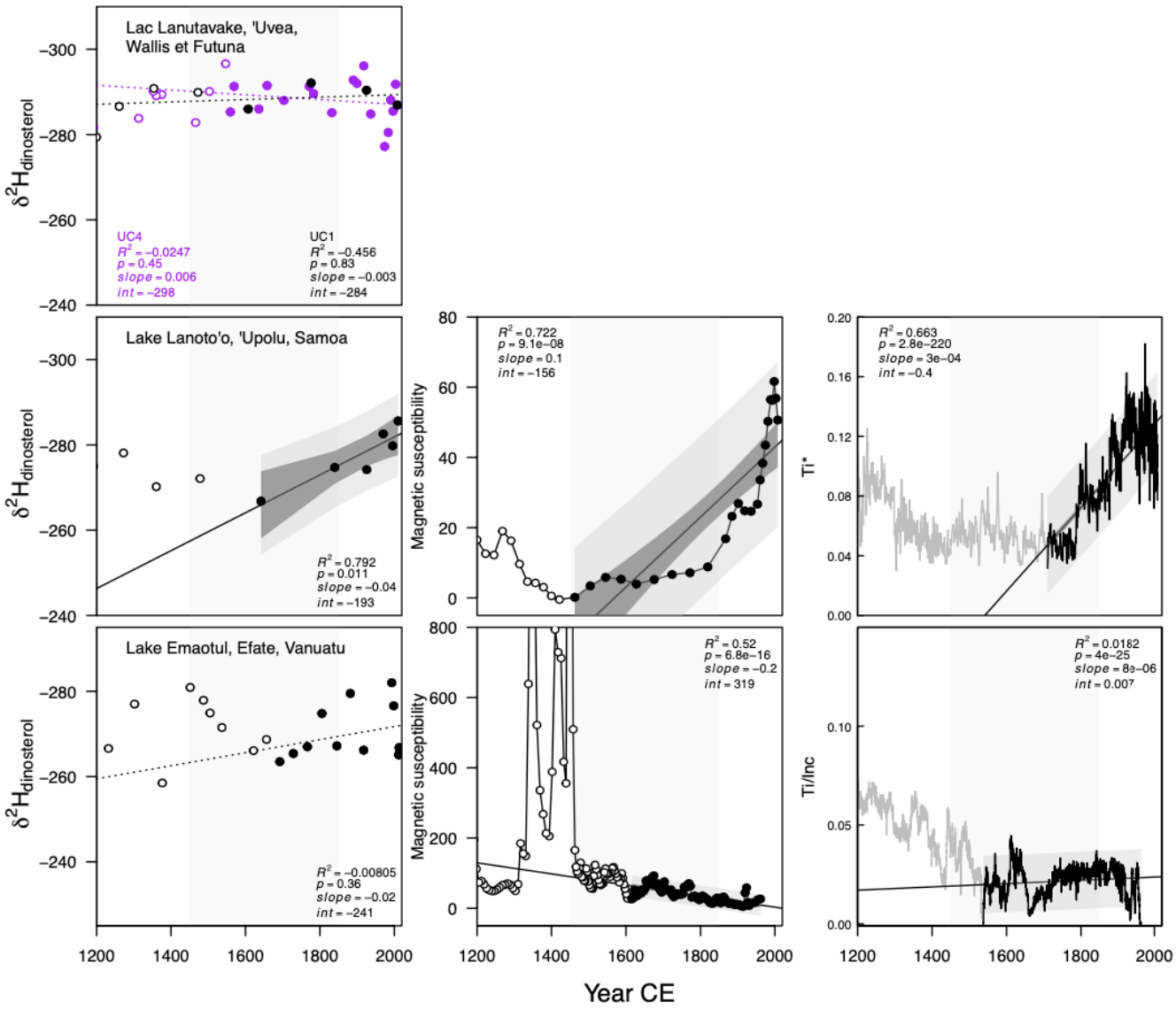

Figure A.9. Testing for changes between LIA and modern in $\delta^2H_{dinosterol}$ data and runoff data. Top panel: Lac Lanutavake ('Uvea, Wallis et Futuna) UC1 and UC4 (note there is no magnetic susceptibility data in the upper portion of these cores sectioned in the field), middle panel: Lake Lanoto'o ('Upolu, Samoa), bottom panel Lake Emaotul (Efate, Vanuatu), note the highest magnetic susceptibility in Lake Emaotul prior to the LIA is from the Kuwae volcanic eruption and there is no runoff data from the interface core G9. Filled circles/black line indicates data points included in regression, selected to include the driest point during the LIA onwards to modern data. Solid regression line indicates correlation significant below the p = 0.01 level, dotted lines indicate correlation not significant. Light gray vertical bar represents the LIA (1450 to 1850).

Appendix A References

Adler, R.F., Gu, G., Huffman, G.J., 2012. Estimating climatological bias errors for the global precipitation climatology project (GPCP). J. Appl. Meteorol. Climatol. 51, 84–99. doi:10.1175/JAMC-D-11-052.1

Adler, R.F., Sapiano, M.R.P., Huffman, G.J., Wang, J.J., Gu, G., Bolvin, D., Chiu, L., Schneider, U., Becker, A., Nelkin, E., Xie, P., Ferraro, R., Shin, D. Bin, 2018. The Global Precipitation Climatology Project (GPCP) monthly analysis (New Version 2.3) and a review of 2017 global precipitation. Atmosphere (Basel). 9. doi:10.3390/atmos9040138

Battarbee, R.W., Jones, V.J., Flower, R.J., Cameron, N.G., Bennion, H., Carvalho, L., Juggins, S., 2001. Diatoms, in: Tracking Environmental Change Using Lake Sediments. Volume 3: Terrestrial, Algal, and Siliceous Indicators. Kluwer Academic Publishers, Dordrecht, The Netherlands, pp. 155–202.

Egbert, G.D., Erofeeva, S.Y., 2002. Efficient inverse modeling of barotropic ocean tides. J. Atmos. Ocean. Technol. 19, 183–204. doi:10.1175/1520-0426(2002)019<0183:EIMOBO>2.0.CO;2

Maloney, A.E., Nelson, D.B., Richey, J.N., Prebble, M., Sear, D.A., Hassall, J.D., Langdon, P.G., Croudace, I.W., Zawadzki, A., Sachs, J.P., 2019. Reconstructing precipitation in the tropical South Pacific from dinosterol $^{2}H/^{1}H$ ratios in lake sediment. Geochim. Cosmochim. Acta 245, 190–206. doi:10.1016/j.gca.2018.10.028

Nozaki, Y., 1997. A fresh look at element distribution in the North Pacific Ocean. Eos Trans. 78, 221. doi:10.1029/97eo00148

Sichrowsky, U., Schabetsberger, R., Sonntag, B., Stoyneva, M., Maloney, A.E., Nelson, D.B., Richey, J.N., Sachs, J.P., 2014. Limnological characterization of volcanic crater lakes on Uvea Island (Wallis and Futuna, South Pacific). Pacific Sci. 68, 333–343. doi:10.2984/68.3.3

Walker, I.R., 2001. Midges: Chironomidae and related Diptera, in: Tracking Environmental Change Using Lake Sediments. Volume 4: Zoological Indicators. Kluwer Academic Publishers, Dordrecht, The Netherlands, pp. 43–66.